frontiers | Frontiers in Energy Research

ORIGINAL RESEARCH
published: 27 May 2022
doi: 10.3389/fenrg.2022.872959

Two-Step Thermochemical CO_2 Splitting Using Partially-Substituted Perovskite Oxides of $La_{0.7}Sr_{0.3}Mn_{0.9}X_{0.1}O_3$ for Solar Fuel Production

Hiroki Sawaguri[1], *Nobuyuki Gokon*[1,2]*, *Kosuke Hayashi*[1], *Yoshikazu Iwamura*[1] and *Daichi Yasuhara*[2]

[1]Graduate School of Science and Technology, Niigata University, Niigata, Japan, [2]Department of Chemistry and Chemical Engineering, Faculty of Engineering, Niigata University, Niigata, Japan

We investigated, herein, the redox activity of partial substitution of the B-site in a series of lanthanum/strontium-manganese-based (LSM) perovskite oxide, $La_{0.7}Sr_{0.3}Mn_{0.9}X_{0.1}O_3$ for solar two-step thermochemical fuel production using concentrated solar radiation as an energy source. We systematically investigated the effects of partial substitution in $LaSrMnO_3$ in terms of their kinetics behavior, oxygen/CO productivity, thermal reduction/oxidation temperatures. Furthermore, repeatability was evaluated and compared among the samples prepared using the same procedure and studied using the same test method. We observed and evaluated the long-term thermal stability of the redox activity and valence variation of the constituting ionic species of the perovskite in the two-step thermochemical CO_2 splitting. From the perspectives of superior activity and long-term repeatability, Ni-, Co-, and Mg-substituted LSM perovskites are promising for thermochemical two-step CO_2/H_2O splitting to produce synthetic gas.

Keywords: thermochemical cycle, CO_2 splitting, redox activity, perovskite oxides, X-ray photoelectron spectroscopy

OPEN ACCESS

Edited by:
Cheng Xu,
North China Electric Power University, China

Reviewed by:
Ivan Ermanoski,
Arizona State University, United States
Alicia Bayon,
Arizona State University, United States
Ellen B. Stechel,
Arizona State University, United States

***Correspondence:**
Nobuyuki Gokon
ngokon@eng.niigata-u.ac.jp

Specialty section:
This article was submitted to Solar Energy, a section of the journal Frontiers in Energy Research

Received: *10 February 2022*
Accepted: *28 April 2022*
Published: *27 May 2022*

Citation:
Sawaguri H, Gokon N, Hayashi K, Iwamura Y and Yasuhara D (2022) Two-Step Thermochemical CO_2 Splitting Using Partially-Substituted Perovskite Oxides of $La_{0.7}Sr_{0.3}Mn_{0.9}X_{0.1}O_3$ for Solar Fuel Production. Front. Energy Res. 10:872959. doi: 10.3389/fenrg.2022.872959

INTRODUCTION

Research in renewable energy sources have been promoted by environmental issues caused by the increase in energy demand and greenhouse gas emissions (Ginley and Cahen, 2011; Lubomirsky and Cahen, 2012; Hussain et al., 2017). The transition from fossil fuels to green energy production is an essential solution to reduce emissions and secure a sustainable energy supply. Solar energy, a free, non-exhaustive, and easily available energy source is the largest exploitable renewable resource that is technically capable of fulfilling all the energy demands of the world.

The combination of concentrated solar radiation as an energy source and thermochemical water/carbon dioxide (CO_2) splitting processes for producing sustainable H_2/carbon monoxide (CO) appear promising for converting solar energy into transportable and storable chemical fuels on demand owing to their high availability. A two-step thermochemical splitting process based on metal oxide accomplishes the splitting of water or carbon dioxide by dividing the difficult thermolysis reaction ($H_2O + \text{heat} \rightarrow H_2 + 1/2O_2$) into two reactions at high temperatures and can be accomplished under less extreme conditions. A two-step thermochemical splitting process using a metal oxide as a redox pair involves the thermal reduction of a metal oxide (M_xO_y) that liberates oxygen from the

metal oxide at a given high temperature (T_1) in **Equation 1**, followed by the oxidation of the reduced metal oxide with steam or carbon dioxide, which yields H_2 or CO and restores the metal oxide to its original state in **Equation 2** at a relatively low temperature (T_2).

Thermal reduction (TR) step:

$$M_XO_Y + \text{heat} \rightarrow M_XO_{Y-\delta} + \delta/2O_2\,(\text{endothermic process}, T_1) \quad (1)$$

Water or CO_2 splitting (WS or CS) step:

$$M_XO_{Y-\delta} + \delta CO_2\,(H_2O) \rightarrow M_XO_Y + \delta CO\,(H_2) + \text{heat}\,(\text{exothermic process}, T_2) \quad (2)$$

where M_xO_y is the corresponding metal oxide, and $M_xO_{y-\delta}$ is the reduced oxide. In an ideal system, these two reactions can be repeated cyclically and indefinitely to produce O_2 and H_2 (or CO) continuously under a supply of the oxidant as a chemical source and heat as an energy source. In addition, the two-step process enables the production of O_2 and H_2 (or CO) in an individual step, eliminating the risk of product recombination at high temperatures. The direct use of concentrated solar radiation as a high-temperature heat source to drive the two-step thermochemical process excludes the use of electricity required in the electrolysis process. Furthermore, the theoretical solar-to-fuel energy conversion efficiency is high (Kim et al., 2012) because the entire spectrum of solar radiation is directly converted into chemical fuels without any expensive catalysts such as the photocatalytic processes (Lange et al., 2014). Thus, using these to decarbonize worldwide energy production is an idea worth considering.

Currently, the main research priorities are the development and evaluation of high performing redox pair materials in the thermochemical cycle to enhance the productivity of H_2 (or CO), design, construction, and evaluation of solar reactor prototypes based on different heating concepts and operation modes (Bulfin et al., 2021). In this context, this study focuses on investigating a highly active redox material to be used in the two-step solar thermochemical process. As such, redox pair materials, metal oxide/metal systems (Schunk et al., 2008; Agrafiotis et al., 2015), such as ZnO/Zn and CdO/Cd, and metal oxide/metal oxide systems, such as Fe_3O_4/FeO, Mn_3O_4/MnO, mixed metal oxide (Tamaura et al., 1995; Miller et al., 2014; Agrafiotis et al., 2015; Sunarso et al., 2017; Randhir et al., 2018) have been extensively investigated. Recently, non-stoichiometric metal oxide systems such as fluorite-based materials of $CeO_2/CeO_{2-\delta}$ and doped-CeO_2 (Meng et al., 2011; Jiang et al., 2014a; Gokon et al., 2015; Marxer et al., 2015; Bhosale and Takalkar, 2018; Lu et al., 2019), and perovskite-based structures of $ABO_3/ABO_{3-\delta}$, in which the oxygen vacancies formed in their structure during the TR step absorb the oxygen from H_2O or CO_2 during the subsequent WS or CS step, resulting in the production of H_2 or CO, respectively. The oxygen non-stoichiometry (δ) governs the productivity of fuel that can be produced by the following two-step thermochemical process using a perovskite oxide (Bayon et al., 2020):

$$ABO_3 + \text{heat} \rightarrow ABO_{3-\delta} + \delta/2O_2 \quad (3)$$

$$ABO_{3-\delta} + \delta CO_2\,(H_2O) \rightarrow ABO_3 + \delta CO\,(H_2) + \text{heat} \quad (4)$$

Here, both cationic sites (A- and B-sites) in a perovskite oxide can be substituted to control the oxygen non-stoichiometry, kinetics, and thermodynamic properties over a wider range. The perovskite oxide remains in the solid state during the two-step process. Their large degree of oxygen non-stoichiometry combined with their structural stability at high temperatures make them attractive redox materials for two-step thermochemical processes (Agrafiotis et al., 2015; Lu et al., 2019).

In previous studies of perovskite-based thermochemical cycles, the following perovskites have been extensively examined for their thermochemical cycles: (La, Sr, Ca)MnO_3 (Scheffe et al., 2013; Demont and Abanades, 2014; Demont et al., 2014; Dey et al., 2015a; Dey et al., 2015b; Demont and Abanades, 2015; Nair and Abanades, 2018; Jouannaux et al., 2019; Riaz et al., 2019; Takalkar et al., 2021), their alumina solid solutions (McDaniel et al., 2013; Deml et al., 2014; Demont et al., 2014; Demont and Abanades, 2015; Gokon et al., 2019; Takalkar et al., 2021) $La_{1-x}A_xMn_{1-y}B_yO_3$ (A = Ca^{2+}, Sr^{2+}, Ba^{2+}; B = Al^{3+} and Ga^{3+}) (Liu et al., 2021), $La_{1-x}Sr_x$ (Mn, Co, Fe) O_3 (Orfila et al., 2016), $La_{0.5}Sr_{0.5}Mn_{1-x}A_xO_3$, (A = Al, Ga, Sc) (Dey et al., 2016), $La_{0.6}Sr_{0.4}Cr_{1-x}Co_xO_3$ (Bork et al., 2015), $La_{1-y}Sr_yCo_{1-x}Zr_xO_3$ (Wang et al., 2020), $La_{1-x}A_xMn_{1-y}B_yO_3$ (A = Ca^{2+}, Sr^{2+}, Ba^{2+}; B = Mg and Al) (Demont and Abanades, 2015), $A_{0.5}Sr_{0.5}MnO_3$ (A = La, Nd, Sm, Gd, Tb, Pr, Dy, and Y) (Takalkar et al., 2019), $Pr_{1-x}Sr_xMnO_3$ (Takalkar and Bhosale, 2019), $LaMO_3$ (M = Co, Fe, Mn, Ni, Al, Cr, Sr) (Takalkar et al., 2020), $La_{0.5}A_{0.5}Mn_{1-y}B_yO_3$ (A = Ca^{2+} and Sr^{2+}; B = Mg, Al, Cr and Ga) (Jouannaux et al., 2019), and $La_{0.6}Sr_{0.4}Mn_{1-x}Fe_xO_3$ (Luciani et al., 2018). In an earlier study, McDaniel et al. (2013) studied the thermochemical two-step H_2O and CO_2 splitting process to examine the redox reactivity of perovskite oxides ($La_{0.6}Sr_{0.4}Mn_{0.6}Al_{0.4}O_3$, $La_{0.4}Sr_{0.6}Mn_{0.6}Al_{0.4}O_3$, and $La_{0.6}Sr_{0.4}Mn_{0.4}Al_{0.6}O_3$) synthesized by the modified Pechini method. It has been reported, in literature, that perovskites demonstrated increased redox activity compared to ceria at the thermochemical cycle at TR temperatures of 1,350°C–1,500°C and a subsequent WS temperature of 1,000°C. Demont et al. (2014) examined the redox performance of perovskites of $La_xSr_{1-x}MnO_3$(LSM) and Ba_xSr_{1-x}(Co, Fe)O_3 and parent structures [Ruddlesden-Popper (RP) phases] for thermochemical two-step water splitting. Perovskites provided larger thermal reduction extents at the modest temperatures than the reference materials of nonstoichiometric compounds such as spinel ferrites or fluorite-structured ceria. However, the reduced sample suffered from hydrogen production in the steam atmosphere during the WS step. Scheffe et al. (2013) performed thermodynamic and experimental investigations of LSM perovskites for the thermochemical splitting of H_2O and CO_2. Literature has reported that strontium contents of x = 0.3 and 0.4 in $La_{1-x}Sr_xMnO_3$ resulted in favorable reduction extents compared to ceria in the temperature range of

TABLE 1 | List of redox performances and reaction conditions for two-step thermochemical cycles using perovskites in previous literatures.

Remarkable Material	Synthesis method	Reactor	Run No.	Reduction temp. (°C)	Re-oxidation temp. (°C)	Reduction duration (min)	Re-oxidation duration [min]	Average O2 productivity (μmol/g)	Average CO (H2) productivity (μmol/g)	CO/O2 ratio (–)	Reference
Y0.5Sr0.5MnO3	Solid-state	TGA	1	1,400	1,100	45	60	481	571	1.19	Dey et al. (2015a)
La0.5Sr0.5MnO3	Solid-state	TGA	1	1,400	1,100	45	60	198	370	1.87	Dey et al. (2015a)
La0.5Sr0.5MnO3	Solid-state	TGA	2	1,400	1,050	45	60	195	242	1.24	Nair and Abanades, (2018)
La0.5Sr0.5MnO3	Solution combustion	TGA	9	1,400	1,000	60	60	128	225	1.76	Takalkar et al. (2019)
Y0.5Sr0.5MnO3	Solution combustion	TGA	9	1,400	1,000	60	60	87	153	1.77	Takalkar et al. (2019)
La0.5Sr0.5Mn0.83Mg0.17O3	Solid-state	TGA	2	1,400	1,050	45	60	170	208	1.22	Demont and Abanades, (2015)
La0.6Sr0.4Al0.6Mn0.4O3	Pechini	TGA	2	1,400	1,050	45	60	200	230	1.15	Demont and Abanades, (2015)
La0.6Sr0.4MnO3	Pechini sol–gel	TGA	1	1,350	1,000	20	50	349	469	1.34	Takalkar et al. (2020)
La0.5Sr0.5Mn0.95Sc0.05O3	Pechini	TGA	3	1,400	1,100	45	45	323	506	1.57	Dey et al. (2016)
La0.5Sr0.5Mn0.75Ga0.25O3	Pechini	TGA	3	1,400	1,100	45	45	264	460	1.74	Dey et al. (2016)
La0.5Sr0.5Mn0.9Mg0.1O3	Pechini	TGA	2	1,400	1,050	45	60	190	215	1.13	Jouannaux et al. (2019)
La0.5Sr0.5Mn0.6Al0.4O3	Pechini	TGA	2	1,400	1,050	45	60	129	205	1.59	Jouannaux et al. (2019)
La0.6Sr0.4Co0.8Cr0.2O3	Pechini	TGA	3	1,200	800	—	60	—	169	—	Bork et al. (2015)
La0.6Sr0.4Co0.8Cr0.2O3	Pechini	TGA	3	1,200	800	—	60	—	(50)	—	Bork et al. (2015)
La0.5Ca0.5Mn0.8Ga0.2O3	Pechini	TGA	2	1,400	1,050	45	60	231	208	0.90	Liu et al. (2021)
LaCoO3	Pechini	TGA	3	1,300	800–1,300	20	60	373	123	0.33	Wang et al. (2020)
LaCo0.9Zr0.1O3	Pechini	TGA	3	1,300	800–1,300	20	60	260	164	0.63	Wang et al. (2020)
LaCo0.7Zr0.3O3	Pechini	TGA	3	1,300	800–1,300	20	60	314	224	0.71	Wang et al. (2020)

1,250°C–1,650°C, but the LSM-based materials did not oxidize stoichiometrically during the WS and CS steps. This could be the reason that the thermodynamics of the LSM for oxidation are unfavorable at higher temperatures than other redox systems (Bayon et al., 2022), but reaction kinetics for oxidation is favorable at high temperature (Gokon et al., 2019). As stated above, at modest temperatures, the redox activity of LSM perovskites exhibited a larger thermal reduction extent than ceria; however, the oxidation extent of LSM perovskites has not been evaluated in earlier studies.

In recent years, in order to explore efficient combinations of cations constituting perovskite oxides, the redox activities of various perovskite oxides have been studied and evaluated by many researchers worldwide. Detail reaction conditions and reactivities of perovskites in the previous studies are summarized in **Table 1** (Dey et al., 2015a; Nair and Abanades, 2018; Demont and Abanades, 2015; Jouannaux et al., 2019; Liu et al., 2021; Dey et al., 2016; Bork et al., 2015; Wang et al., 2020; Takalkar et al., 2019; Takalkar et al., 2020). The impacts of A- or B-site substitution of Mn-based perovskite on CO and H_2 production in the thermochemical processes were studied and reported in this research field. The redox activity for CO_2 splitting was examined for partially substituted perovskites, in which Mn was the single reducible cation and the Mn^{4+}/Mn^{3+} redox pair was activated in the oxygen exchange process. The structural evolution and thermochemical behavior are discussed. Different cation combinations of B-sites in La(B, B') O_3 (B and B' = Mn, Co, Ni) and of the A-site in the (AA') (BB')O_3 (A and A' = La, Sr, Ca; B and B' = Mn, Fe, Co) and partial substitution of the B-site in some LaMn-perovskites exhibited significant CO productivity for thermochemical CO_2 splitting (Nair and Abanades, 2018). However, the production ratio of O_2/CO < 2 remained for all the samples tested in **Table 1**. Even in other perovskites with B-site partial substitution of low content, $La_{0.6}Sr_{0.4}Cr_{0.8}Co_{0.2}O_3$ (Bork et al., 2015), $La_{0.6}Ca_{0.4}Mn_{0.8}Ga_{0.2}O_3$ (Liu et al., 2021), $La_{0.5}Sr_{0.5}Mn_{0.95}Sc_{0.05}O_3$ (Dey et al., 2016), $La_{0.5}Sr_{0.5}Mn_{0.75}Ga_{0.25}O_3$ (Dey et al., 2016), $LaCo_{0.9}Zr_{0.1}O_3$, and $LaCo_{0.7}Zr_{0.3}O_3$ (Wang et al., 2020), they reported that the redox performance was improved in comparison to the non-substituted materials. Therefore, there is a possibility that the substitution of low content for B-sites in perovskite oxides is promising for enhancing the redox activity of the materials.

At present, $La_xSr_{1-x}Mn_{1-x}Al_xO_3$, $La_ySr_{1-y}Mn_yAl_{1-y}O_3$, and $La_{0.7}Sr_{0.3}Mn_{1-z}Cr_zO_3$ series were systematically studied to improve the reactivity of LaMn-based perovskite in the TR and WS steps of a two-step thermochemical water-splitting cycle for hydrogen production (Gokon et al., 2019; Gokon et al., 2020). The effect of partial substitution of the A-site ($La_{0.7}A_{0.3}Mn_{0.9}Cr_{0.1}O_3$, A = Ba, Sr, Ca) on thermochemical H_2O/CO_2 splitting was studied and presented at the SolarPACES conference in 2021 (Sawaguri et al., 2021). The 10%–20% Cr substitution at the B-site of LSM perovskites enhanced the kinetics of the oxidation step of the two-step thermochemical cycle and improved the productivity of H_2 in comparison to the Al-substituted LSMs (Gokon et al., 2019). In addition, we reported that $La_{0.7}Sr_{0.3}Mn_{0.9}Cr_{0.1}O_3$ (LSMC7391) has an equivalent oxidation activity for H_2O and CO_2 splitting processes in the thermochemical cycle (Sawaguri et al., 2020). The results indicate that partial substitution with a small content at the B-site is available to improve the reactivity of LSM perovskite for a two-step thermochemical cycle, and the CO_2/H_2O splitting process to produce syngas (a gas mixture of H_2 and CO) can be operated using the redox material through a two-step thermochemical H_2O/CO_2 splitting cycle.

According to the report of the literature as described above, the emerging LSM perovskite can be found by partial substitution by different ion species with low content incorporated into manganese-rich LSM perovskite. However, to the best of our knowledge, 1) the effects of partial substitution with a small content at the B-site in the LSM perovskite have not been evaluated, and compared at the same substitution level with systematic variation of ion species (for example, $La_{0.7}Sr_{0.3}Mn_{0.9}X_{0.1}O_3$); 2) the valence variations of the substituted ion species in the redox process have not been focused except for Mn at the B-site of LSM perovskites; 3) there are limited evaluations with regard to long-term redox activity and thermal stability of the partially substituted LSM (McDaniel et al., 2013; Takalkar et al., 2021). Herein, following this approach and under the same test conditions using a test equipment, the authors investigated and evaluated the oxygen and CO productivity and kinetics of the respective steps, the optimization of TR and CS step temperatures, and the repeatability of the two-step CO_2 splitting thermochemical cycle based on partial substitution of the B-site with low content X in the LSM perovskite oxides $La_{0.7}Sr_{0.3}Mn_{0.9}X_{0.1}O_3$ (X = Mg, Al, Cr, Fe, Co, Ni, Cu, Ga) with various ionic species. In addition, the authors studied and evaluated the repeatability of oxygen and CO productivity and thermal stability in a long-term redox test. For one of the best performance samples, the valence variations of all ionic species constructing the partially substituted LSM perovskite were experimentally estimated, and the role of the partially substituted ion species was experimentally observed and elucidated for the samples that were synthesized, thermally reduced, and oxidized in the thermochemical cycle.

EXPERIMENTAL SECTION

Material Preparation

$La_{0.7}Sr_{0.3}Mn_{0.9}X_{0.1}O_3$ perovskite oxides were synthesized using the modified Pechini method (Pechini, 1967). First, stoichiometric molar ratio of each perovskite material was dissolved in distilled water with metal nitrate. The reagents used in this study were $La(NO_3)_3{\cdot}6H_2O$ (Wako, 99.9% purity), $Sr(NO_3)_2$ (Wako, ≥98.0% purity), $Cr(NO_3)_3{\cdot}9H_2O$ (Strem Chemicals, 99.9% purity), $Mn(NO_3)_3{\cdot}6H_2O$(Wako, ≥98.0% purity), $Mg(NO_3)_2{\cdot}6H_2O$ (Wako, ≥98.0% purity), and $Cu(NO_3)_2{\cdot}3H_2O$ (Wako, 99.9% purity), $Fe(NO_3)_3{\cdot}9H_2O$ (Kanto Chemical, ≥99% purity), $Co(NO_3)_2{\cdot}6H_2O$ (Kanto Chemical, ≥98% purity), $Ni(NO_3)_3{\cdot}6H_2O$ (Wako, 99.9% purity), and $Ga(NO_3)_3{\cdot}8H_2O$ (Kishida Chemical, ≥99% purity). Citric acid (Wako, ≥98.0% purity) and ethylene glycol (Wako, ≥99.5% purity) were added and dissolved in an aqueous solution. The molar ratio of the total amount of metallic cations, citric acid,

and ethylene glycol was 1:5:5. These solutions were stirred and heated at 80°C for 1-h in an oil bath to evaporate water and then heated at 170°C for gel formation. The obtained gel was dried at 300°C for 5-h in an electric oven. The resulting precursor was pulverized using a mortar and pestle, and calcined at 1,200°C for 8-h in a muffle furnace. The following powder-like materials were synthesized: $La_{0.7}Sr_{0.3}Mn_{0.9}X_{0.1}O_3$ (X = Mg, Al, Cr, Fe, Co, Ni, Cu, and Ga).

Powder X-ray diffraction (XRD) was performed using a Bruker D2 PHASER with Cu Kα radiation (λ = 0.15418 nm, 30 kV–10 mA) at room temperature for crystallographic phase identification of the synthesized materials and materials obtained after thermochemical testing. Diffraction data were collected with an angular range of 2θ = 20°–80°, step interval of 0.02°, and recording time of 1 s. The crystalline phases were identified by comparison with standard reference databases [Inorganic Crystal Structure Database (ICSD) and Crystallography Open Database (COD)]. Rietveld refinement was performed using the whole pattern fitting (WPF) method of the FullProf package to evaluate the space group, crystal system, and lattice parameters of the synthesized materials.

Scanning electron microscopy (SEM, JCM-6000, JEOL) with an acceleration voltage of 15 kV was used to observe the powder morphology and size before and after the redox activity test of the thermochemical cycle.

X-ray photoelectron spectroscopy (XPS) analysis was performed using a Quantum 2000 (ULVAC-PHI. Inc.) with an aluminum anode (Al Kα, 25 W (15 kV, 1.67 mA), hv = 1,486.6 eV) to evaluate the valence states of the elements. For energy calibration of the XPS spectrum, the authors used the adventitious carbon C1s peak at 284.8 a of binding energy. The Gaussian function for peak fitting of the XPS spectrum, Shirley method (Shirley, 1972) for the baseline of the XPS spectrum, and the Savitzky–Golay method (Press and Teukolsky, 1990) for data smoothing of the XPS spectrum were used for analysis of the XPS spectrum.

Redox Activity and Repeatability Tests of the Synthesized Perovskite Oxides

The redox reactivity of $La_{0.7}Sr_{0.3}Mn_{0.9}X_{0.1}O_3$ perovskite oxides was evaluated through oxygen/carbon monoxide (CO) productivity, kinetics, and TR/CS temperature impacts for two-step thermochemical CO_2 splitting cycling. The redox activity performance was examined using a thermogravimetric reactor (NETZSCH STA2500 Regulus, weight resolution of 0.03 μg, temperature resolution of 0.3 K) equipped with a type S thermocouple (temperature resolution of ±0.0025 × |t| °C) for endothermic thermal reduction (TR) and subsequent exothermic carbon dioxide splitting (CS) steps of the sample powder.

In the thermogravimetric reactor used in our laboratory, O_2 gas evolved during the TR steps is quickly removed upward by gas flow from below the balance. However, the upward stream of gas flow is a disadvantage with regard to contacting CO_2 with the sample during the CS step. In order to estimate the impacts on the rates and amounts of O_2 release and CO production affected by gas diffusion limitations owing the sample mounting and gas flow orientation in the reactor, before starting the present study, the authors examined redox reactivity using some samples with different amounts (heights) and different sizes of platinum pan in order to determine the experimental procedure. As the results, the authors found that the present test conditions can realize reversible redox reaction under the gas flow orientation without governing diffusion limitation of CO_2 supply in the preliminary test. In the preliminary test, a blank test without any sample in a Pt pan was performed in order to check general drift of balance in the thermogravimetric reactor under the experimental procedure of redox reactivity test. The weight change of 0.0274% was observed in the test. Thus, an influence of general drift owing to equipment was relatively small compared with weight change derived from redox reaction.

The reactivity test was performed using the following procedure: Approximately 50 mg of sample powder was packed into a platinum pan (inner diameter of 5.2 mm, height of 2.6 mm) and mounted on the balance in a tubular ceramic chamber of the reactor. To eliminate adsorptive species on the surface of the sample powder, such as water, CO_2, and O_2, the sample powder was first heated at 300°C for 0.5-h at a rate of 50 K/min using an electric furnace while passing 99.999% high-purity nitrogen gas through the reactor at a flow rate of 100 cm^3/min at standard state (unit of sccm). Subsequently, the sample powder was subjected to the TR step at 1,200°C–1,400°C for 1.5-h to thermally release oxygen from the sample power. The temperature of the sample powder was monitored using an S-type thermocouple in contact with the bottom of the platinum pan. The powder was cooled at 800°C–1,200°C at a rate of 20 K/min under a N_2 flow, as indicated above. The passing gas was switched into a gas mixture with a N_2 flow rate of 50 sccm and a CO_2 flow rate of 50 sccm to perform the CS step. The sample was maintained at 800°C–1,200°C for 0.5-h in the electric furnace of the reactor to complete the CS step. The TR and CS steps for the reactivity tests were repeated four times. The temperature impacts were evaluated by testing five times in sequence with the temperatures of the TR and CS steps. The sample powder weight changed in the reactor furnace by O_2 release during the TR step and O_2 uptake from CO_2 during the CS step. The weight change of the sample was recorded as a function of time to monitor the fractional extent of the reaction in the TR and CS steps.

The repeatability of the redox reaction for the sample power was evaluated using a thermogravimetric reactor using the following procedure. The TR step was performed at 1,400°C at a N_2 flow rate of 100 sccm for 10 min, and subsequently, the CS step was conducted at 1,200°C at a gas mixture flow rate of 100 sccm (CO_2 50% and N_2 50%) for 15 min. The TR and CS steps were repeated 50 times in sequence to examine the repeatability of O_2 release and CO production.

O_2 and CO productivity per sample weight [n_{O2} and n_{CO} (mol/g)] were calculated using the molar weight of the oxygen atom [M_O (g/mol)], weight change of the sample [Δm (g)], and sample weight at time t = 0 [m_s (g)]. The weight change of the sample (Δm) during the TR and CS steps was calculated from the weight decrease and increase, respectively. The O_2 and CO production rates per sample weight [r_{O2} and r_{CO} (mol/g)]

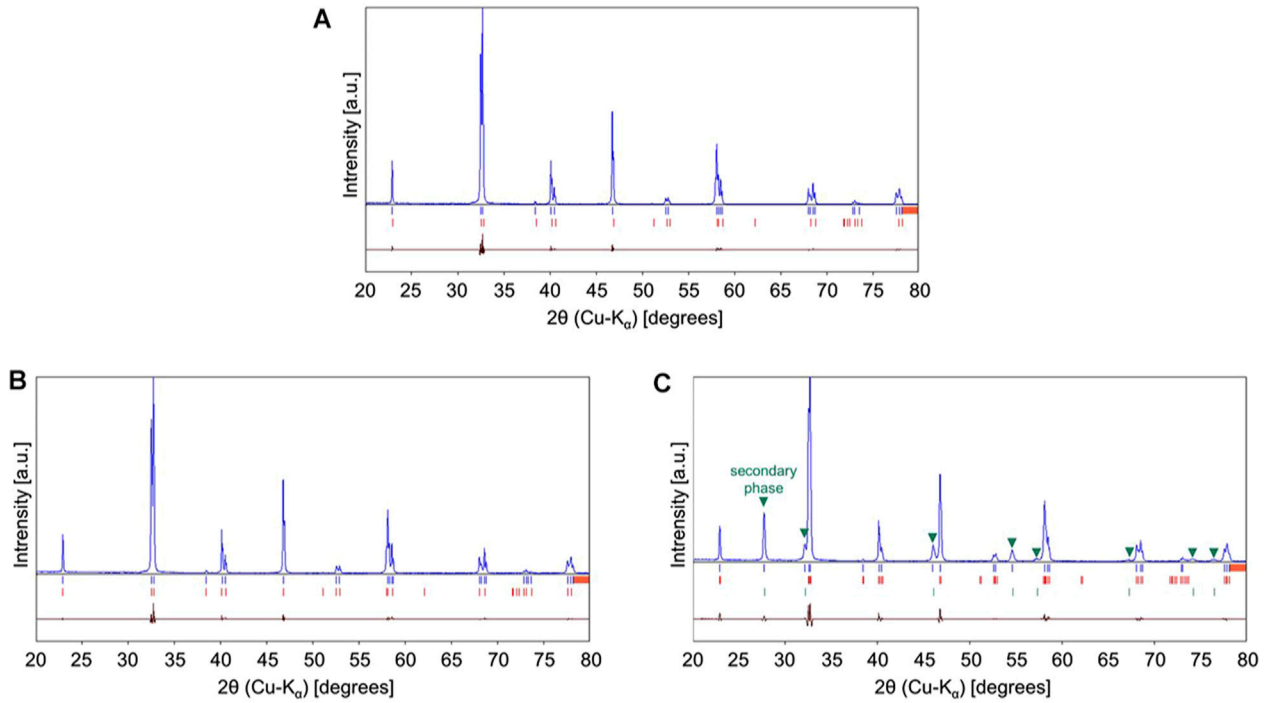

FIGURE 1 | XRD patterns of $La_{0.7}Sr_{0.3}Mn_{0.9}X_{0.1}O_3$ [X = **(A)** Mn (non-substituted LSM), **(B)** Co-substituted LSM, and **(C)** Ce-substituted LSM]. The blue and red vertical bars below the XRD pattern corresponded to peak positions of sample and crystalline phase in the reference, respectively. The signal pattern of dark red represented the relative difference of intensity between the sample and reference in the Rietveld refinement.

TABLE 2 | Substitution cation (X), space group, crystal system, and lattice parameters of refined structured of X-substituted LSMs.

substituted cation X	Space group	Crystal system	Lattice pammeters (Å)			Reference	COD data No. (ICSD code)
			a	b	c		
Mn (non-substitution)	R-3c (167)	Trigonal	5.508(2)	5.508(2)	13.368(2)	Petrov et al. (1999)	(50717)
Mg	R-3c (167)	Trigonal	5.499(7)	5.499(7)	13.345(3)	Troyanchuk et al. (2015)	(258933)
Al	R-3c (167)	Trigonal	5.478(4)	5.478(4)	13.484(8)	Mostafa et al. (2008)	(245860)
Cr	R-3c (167)	Trigonal	5.507(3)	5.507(3)	13.355(9)	El-Fadli et al. (2002)	4002477
Fe	R-3c (167)	Trigonal	5.514(0)	5.514(0)	13.370(5)	Yanchevskii et al. (2006)	(155210)
Co	R-3c (167)	Trigonal	5.504(4)	5.504(4)	13.348(3)	El-Fadli et al. (2002)	(94794)
Ni	R-3c (167)	Trigonal	5.497(6)	5.497(6)	13.337(4)	Reshmi et al. (2013)	(188747)
Cu	R-3c (167)	Trigonal	5.503(6)	5.503(6)	13.342(9)	El-Fadli et al. (2002)	(188212)
Ga	R-3c(167)	Trigonal	5.509(8)	5.509(8)	13.362(5)	El-Fadli et al. (2002)	(94799)
Ce	R-3c (167)	Trigonal	5.500(9)	5.500(9)	13.377(1)	Paiva-Santos et al. (2002)	1532010
—	Fm-3m (225)	Cubic	5.572(4)	5.572(4)	5.572(4)	Wu et al. (2014)	(291250)

were calculated from the time derivative of weight m (g) at time $t = t$ (dm/dt), as represented in **Eqs 7**, **8**.

$$n_{O2} = \frac{\Delta m}{2 \times M_O \times m_s} \quad (5)$$

$$n_{CO} = \frac{\Delta m}{M_O \times m_s} \quad (6)$$

$$r_{O2} = -\frac{dm/dt}{2 \times M_O \times m_s} \quad (7)$$

$$r_{CO} = \frac{dm/dt}{Mo \times m_s} \quad (8)$$

RESULTS AND DISCUSSION

Thermochemical Redox Activity Test for $La_{0.7}Sr_{0.3}Mn_{0.9}X_{0.1}O_3$

Figure 1 illustrates the XRD patterns of $La_{0.7}Sr_{0.3}Mn_{0.9}X_{0.1}O_3$ [X = Mn (non-substituted LSM), Co-substituted LSM, and Ce-substituted LSM] at room temperature in the 2θ range. The XRD data for the other samples are shown in **Supplementary Figure S1**. The lattice parameters and space groups of the synthesized $La_{0.7}Sr_{0.3}Mn_{0.9}X_{0.1}O_3$ were determined by Rietveld refinement. All diffraction peaks assigned to the crystalline phase

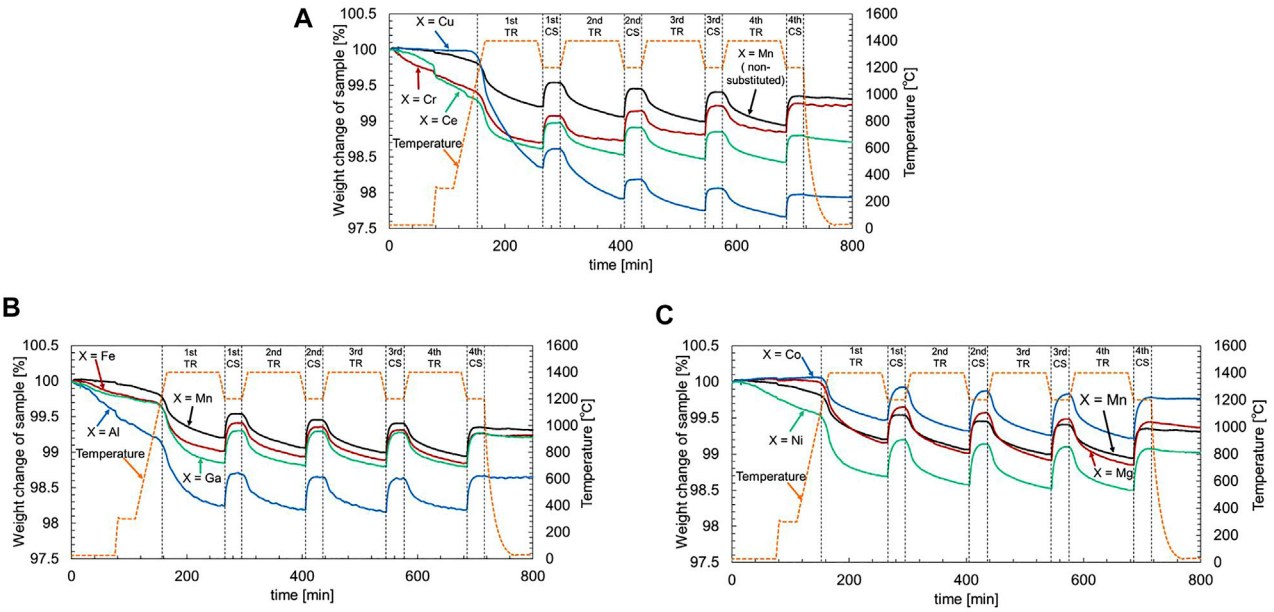

FIGURE 2 | TGA profiles of the weight change in the activity tests of two-step thermochemical CO_2 splitting using $La_{0.7}Sr_{0.3}Mn_{0.9}X_{0.1}O_3$ sample powder [X = **(A)** Cu, Cr, and Ce-substituted LSMs, **(B)** Fe, Al, and Ga-substituted LSMs, and **(C)** Co, Ni and Mg-substituted LSMs]. For comparison, TGA profile of Mn (non-substituted LSM) is plotted in the figure. To eliminate adsorptive species on the surface of the sample powder, the sample powder was first heated at 300°C for 0.5-h at a rate of 50 K/min using an electric furnace while passing 99.999% high-purity nitrogen gas through the reactor at a flow rate of 100 cm^3/min at standard state. Subsequently, the activity tests were continuously repeated four times under the same condition to evaluate the repeatability.

were indexed in a trigonal unit cell [space group R- 3C (167)], and the lattice parameters are listed in **Table 2** (Petrov et al., 1999; Troyanchuk et al., 2015; Mostafa et al., 2008; El-Fadli et al., 2002; Yanchevskii et al., 2006; Reshmi et al., 2013; Paiva-Santos et al., 2002; Wu et al., 2014). As seen in the XRD pattern of the non-substituted LSM (**Figure 1A**), a series of peaks (blue vertical bars) correspond to the crystalline phase (red vertical bars below the XRD pattern), as cited in (Petrov et al., 1999). In addition, no secondary phases were observed in the pattern. As seen in **Figure 1B, a** series of peaks for Co-substituted LSM are identical to the crystalline phase with the same index as the Co-substituted reference (red vertical bars below the XRD pattern). The lattice parameter of the Co-substituted LSM is smaller than that of the non-substituted LSM (**Table 2**), because ionic radius of Co cation (Co^{3+}: 0.61 Å, 6 coordination by O^{2-} ion) is smaller than Mn cation (Mn^{3+}: 0.645 Å, at high spin and 6 coordination by O^{2-} ion) (Shannon and Prewitt, 1969). The XRD peaks for the Co-substituted LSM were shifted toward greater diffraction angles than those of the non-substituted LSM. The results indicate that the Co-substituted LSM was successfully synthesized as a solid solution of the perovskite structure without impurities. However, in the XRD pattern of the Ce-substituted LSM (**Figure 1C**), $La_{0.64}Sr_{0.36}MnO_3$ [a trigonal unit cell, space group R- 3C (167)] (Paiva-Santos et al., 2002), and $La_2Ce_2O_7$ [cubic unit cell, space group Fm-3m (225)] (Wu et al., 2014) were observed. The result indicates that Ce cation is not incorporated into a perovskite structure of non-substituted LSM owing to relatively large ionic radius of Ce cation (Ce^{3+}: 1.034 Å, Ce^{4+}: 0.87 Å in 6 co-ordination by O^{2-} ion) compared with Mn cation (Mn^{3+}: 0.645 Å at high spin and 0.58 Å at low spin in 6 co-ordination by O^{2-} ion) (Shannon and Prewitt, 1969). Except for the Ce-substituted LSM, all sample powders were successfully synthesized as a single phase in a trigonal unit cell [space group R-3C (167)]. The XRD patterns of as-synthesized sample and sample obtained after the redox activity test are shown in lower and upper side of **Supplementary Figure S1**. The original crystalline phase was maintained for the sample obtained after the redox activity test, except of Cu-substituted sample. The XRD peak at the $2\theta = 28^{\circ}$ observed for the sample obtained after the redox activity test were due to glass holder made by Si in the XRD measurement (COD data No. 9013105) (Dutta, 1962).

Figure 2 displays the TGA profiles of the weight change in the activity tests of two-step thermochemical CO_2 splitting using $La_{0.7}Sr_{0.3}Mn_{0.9}X_{0.1}O_3$ sample powder. The first run of all TGA profiles was excluded from analysis and discussion of the test results because the result in the first run might include non-reproducible effects of sample and TGA reactor preparations (moisture and air adsorbed on the surface of sample powder, and contamination in the TGA reactor). As shown in **Figure 2A**, the non-substituted LSM gradually decreased with time during the TR step and rapidly increased during the subsequent CS step. The variation in weight change was reproducibly repeated in the second to fourth runs. For the Cr-substituted LSM, we observed that the weight gain gradually increased during the CS step of the second to fourth runs when the run number increased. This result indicates that the Cr substitution into LSM perovskite contributes to the reaction rate of the oxidation

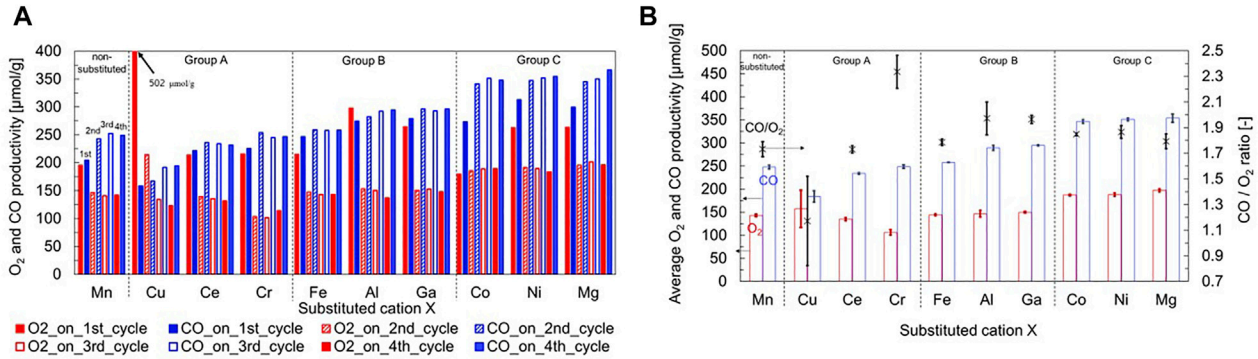

FIGURE 3 | (A) O_2 and CO productivities of all samples during the first to fourth runs and **(B)** average values of O_2 and CO production and CO/O_2 ratio in the second to fourth runs of the two-step thermochemical CO_2 splitting activity tests.

reaction during the CS step. In the case of the Ce-substituted LSM, the behavior of the weight loss and gain during the second to fourth runs was repeatedly observed with similar levels of the non-substituted LSM. However, the Cu-substituted LSM showed that the weight loss during the TR step was greater than the weight gain during the CS step in first to second runs. The results indicate that Cu-substituted LSM partially decomposed into solid phases, providing irreversible redox properties in cyclic activity tests of two-step thermochemical CO_2 splitting. The XRD patterns of the synthesized Cu-substituted LSM and the material obtained after the activity test are shown in **Supplementary Figure S2**. As seen in **Supplementary Figure S2A**, the as-prepared sample is a single solid phase with a trigonal unit cell (space group R- 3C (167)), as listed in **Table 2**. After the activity test (**Supplementary Figure S2B**), the material was composed of a solid mixture of $La_{0.67}Sr_{0.33}MnO_3$ [a trigonal unit cell, space group R- 3C (167), COD data No. 1533312] (Zhang et al., 2003) and $La_{1.5}Sr_{0.5}Mn_{0.5}Cu_{0.5}O_4$ (a tetragonal unit cell, space group I4/mmm (139), COD data No. 4002411) (McCabe and Greaves, 2006). In previous studies, reversible or irreversible phase transition were observed when perovskites were heated at high temperatures (Vogt and Schmahl, 1993; Chen et al., 2014). Ideally, the molar ratio of oxygen atom in RP1 structure [A_2BO_4, oxygen/(metal cation) = 4/3] is less than that of the perovskite structure [ABO_3, oxygen/(metal cation) = 3/2]. The large weight loss of Cu-substituted LSM during the TR step may include the irreversible phase transition of the perovskite structure into the PR1 and thermal reduction of perovskite structure. Furthermore, there is a possibility that a vaporization of Cu-substituted sample occurs at high temperature. The incomplete redox reaction of Cu-substituted LSM may be that the latter solid phase ($La_{1.5}Sr_{0.5}Mn_{0.5}Cu_{0.5}O_4$) was not oxidized with CO_2 under the present test conditions. The TGA profiles of the Al-, Fe-, and Ga-substituted LSMs are shown in **Figure 2B**, and as a reference, the results of the non-substituted LSM are also plotted in the figure. The loss and gain in weight were reproducibly observed during the second to fourth runs of the two-step thermochemical CO_2 splitting activity tests. The extent of weight loss during the TR step for all samples was approximately the same as that of the non-substituted LSM, while that of the weight gain was greater than that of the non-substituted LSM and Cr- and Ce-substituted LSMs. **Figure 2C** illustrates the TGA profiles of the Mg-, Co-, and Ni-substituted LSMs. The weight change for all samples during the second to fourth runs was significantly greater than that for the non-substituted LSM. In addition, the loss and gain in weight were reproducibly observed. These results indicate that $La_{0.7}Sr_{0.3}Mn_{0.9}X_{0.1}O_3$ samples (except for Cu-substituted LSM) have high thermal stability and reactivity without degradation and sufficient repeatability for thermochemical CO_2 splitting under the present reaction conditions.

Figure 3A shows the O_2 and CO productivities of all samples during the first to fourth runs of the two-step thermochemical CO_2 splitting activity tests. Each value of productivity was calculated from the extent of the weight change in **Figure 2**. The non-substituted LSM demonstrated stable and reproducible O_2 and CO productivities in the second to fourth runs. The amounts of O_2 and CO produced were approximately 140 and 250 μmol/g-material, respectively. The authors categorized them into three groups in order of productivity: group A = Cu, Ce, and Cr (low productivity); group B =Fe, Al, and Ga (middle productivity); group C = Co, Ni, and Mg (high productivity levels). In group A, the O_2 and CO productivities were equivalent for Ce-substituted LSM or lower for Cr-substituted LSM than that of non-substituted LSM during the second to fourth runs. For group B, the O_2 productivity of the substituted LSM was similar to that of the non-substituted LSM, while the CO productivity was approximately the same or slightly higher than that of the non-substituted LSM during the second to fourth runs. In the case of group C, both productivities were higher than that of the non-substituted LSM during the second to fourth runs.

The average values of O_2 and CO production and CO/O_2 ratio in the second to fourth runs are shown in **Figure 3B**. In group A, O_2 production decreased in the order of Cu-, Ce-, and Cr-substituted LSMs, while CO production and CO/O_2 ratio increased. The average values of O_2 and CO production in the second to fourth runs for the Cr-substituted LSM were 106 and 248 μmol/g-material, respectively. The CO/O_2 (CO/O_2 = 2.33) value exceeded the stoichiometric ratio (CO/O_2 = 2). The results indicate that a large extent of thermal reduction obtained at the

TR step of first run was oxidized through the CS step of the second to fourth runs. The CO/O_2 ratios of Cu-, and Ce substituted LSMs were lower than the stoichiometric ratio of 2. The results indicate that Cr substitution may improve CO production when the stoichiometric ratio increases as the number of runs increase. For group B, the average values of O_2 and CO production in the second to fourth runs were 145–150 (143 for non-substituted LSM) and 258–295 (248 for non-substituted LSM) μmol/g-material, respectively. The CO production was in order of Fe < Al < Ga, and CO/O_2 ratio was 1.79 (Fe-substitution), 1.97 (Al-substitution), and 1.96 (Ga-substitution). The results indicate that Al and Ga substitutions at the B-site of LSM enhanced CO production in the CS step. Shannon's literature reported that Al and Ga ions normally have a common valence number of 3+ in 6 co-ordination by O^{2-} ions (Shannon and Prewitt, 1969). The following assumption is considered from the above results: when the valence number of substitution Al and Ga ions does not vary, thereby retaining the valency in the LSM perovskite structure, the substitution ion may promote thermal reduction of Mn ions in the LSM perovskite structure, while it plays a role in stabilizing the crystal structure with oxygen vacancies formed by the TR step. Then, in the subsequent CS step, the low-to-high valency transition of Mn ions in the LSM perovskite structure can be enhanced during the CS step.

In the case of group C, the O_2 production level of 188–197 μmol/g-material was the highest among all the samples tested in this study. The average CO production was 347 μmol/g-material for Co substitution, 351 μmol/g-material for Ni substitution, and 354 μmol/g-material for Mg substitution. Among all the samples, these three substituted LSMs exhibited similar O_2 and CO production levels. The CO/O_2 ratio was 1.85 (Co-substitution), 1.87 (Ni-substitution), and 1.79 (Mg-substitution). The impact of the test temperature on the O_2 and CO productivities is evaluated in the subsequent section. The results of group C indicate that Co, Ni, and Mg substitutions at the B-site of LSM enhanced both O_2 production during the TR step and CO production during the subsequent CS step. These ion species have a common valence number of 2+ in 6 coordinated by O^{2-} ions. In contrast, Co and Ni ions can also have valence numbers of 3+ and 4+ in 6 co-ordination by O^{2-} ions (Shannon and Prewitt, 1969). The following supposition is made for the Mg-substituted LSM: the lattice volume of the Mg-substituted LSM is smaller than that of the non-substituted LSM (**Table 2**). This result means that an ion species smaller than the Mn ion is substituted into the B-site of the LSM perovskite. However, the ionic radius (0.720 Å) of Mg^{2+} in 6 coordination by O^{2-} ion is the greatest among those of Mn ions with various valence numbers in six coordination. Thus, from the viewpoint that substitutional solid solution is formed in the Mg-substituted LSM perovskite oxide, the Mg ion has a small coordination number (<6), leading to a small ionic radius at retaining the Mg^{2+} state, or high valence numbers of Mn ions are induced owing to charge balance by Mg^{2+} substitution at the B-site. The variation of O^{2-} coordination or high valency Mn ions may enhance the mobility of O^{2-} ions in the crystal structure at high temperatures, leading to improved O_2 production during the TR step. As a result, the reduced phase containing oxygen vacancies in the Mg substitution of LSM perovskite contributes to the enhancement of CO production compared to the non-substituted LSM. Further investigations about kinetics of mobility of O^{2-} ion during the TR step are required to elucidate the detailed mechanism.

Figure 4A illustrates the O_2 production profiles of samples belonging to group A during the TR step in the first to fourth runs. When the temperature of the sample reached 1,400°C, the production rate of O_2 reached a maximum in all runs. The peak rates of O_2 production for non-substituted LSM were 6.5–6.7 μmol/(min·g-material) in the second to fourth runs. For the Cu-substituted LSM, the peak rate of O_2 production in the first run increased because of the irreversible decomposition of the solid phase. The peak rates of O_2 production in the second to fourth runs gradually decreased in comparison with the non-substituted LSM. The peak rates of the Cr- [5.1–6.5 μmol/(min·g-material)] and Ce-substituted LSMs [6.5–6.8 μmol/(min·g-material)] in the second to fourth runs were similar to the non-substituted LSM in each run. Thus, the substitution ions of group A did not affect the production rate of O_2 during the TR step of the two-step thermochemical CO_2 splitting cycle. **Figure 4A** illustrates the O_2 production profiles of samples belonging to group B during the TR step in the first-fourth runs. The peak rates of Fe-(7.2–7.4 μmol/(min·g-material)), Al-(7.3–8.7 μmol/(min·g-material)), Ga-substituted LSMs (8.1–8.2 μmol/(min·g-material)) were higher than those of non-substituted LSM in second to fourth runs. The decay trend of O_2 production after the peak rate for the samples in group B was similar to that of the non-substituted LSM. The results indicated that the substitution ions of group B enhanced the peak rate of O_2 production during the TR step. The O_2 production profiles of samples belonging to group C are shown in **Figure 4C**. The peak rates of Co-(9.3–10.2 μmol/(min·g-material)), Ni-(9.7–10.3 μmol/(min·g-material)), Mg-substituted LSMs (9.6–10.1 μmol/(min·g-material)) were highest among the samples tested in this study. The peak rates of group C were 1.4–1.6 times greater than those of non-substituted LSM. There was little difference in the decay trend of O_2 production in group C. The results indicated that the substitution ions in group C contributed to the enhancement of the production rate.

Figure 5A shows the CO production profiles of samples belonging to group A during the subsequent CS step in the first to fourth runs. The CO production for all samples tested in this study was immediately initiated at the target temperature when the gas stream was switched to a gas mixture of N_2 and CO_2. The peak rates of CO production for the non-substituted LSM were 69.8–70.8 μmol/(min·g-material) in the second to fourth runs. The time required for CO production was approximately 20 min. The order of peak rates of the CO production is Cu-(61.4–78.0 μmol/(min·g-material)), Cr-(71.7–75.9 μmol/(min·g-material)), and Ce-substituted LSMs (80.8–82.3 μmol/(min·g-material)) in second to fourth runs. The peak rates of the Cr- and Ce-substituted LSMs were higher than those of the non-substituted LSM in the second to fourth runs. The results of the Cr substitution agreed with the previous results that the Cr substitution in LSM enhanced the oxidation rate of the reduced material during the WS step of two-step thermochemical water-

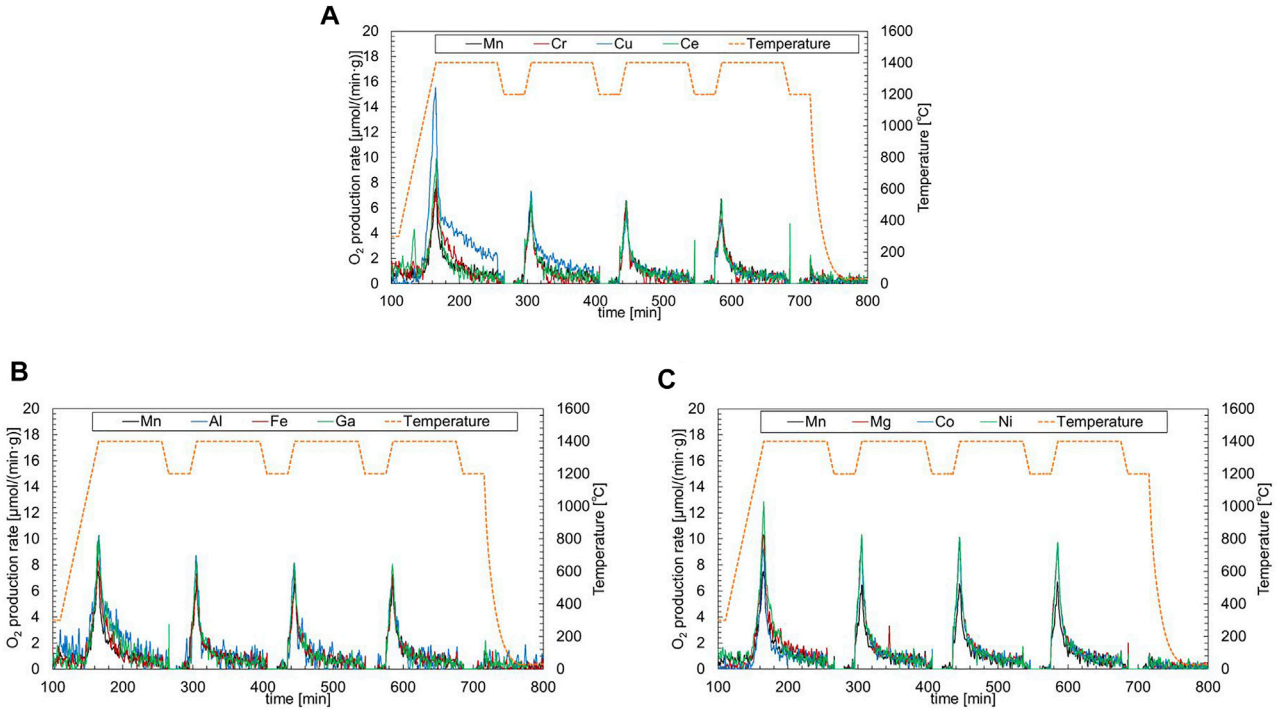

FIGURE 4 | O_2 production profiles of samples belonging to **(A)** group A (Cu, Cr, and Ce-substituted LSMs), **(B)** group B (Fe, Al, and Ga-substituted LSMs), and **(C)** group C (Co, Ni and Mg-substituted LSMs) during the TR step in the first to fourth runs. The production profiles correspond to left Y-axis, while the temperature profile corresponds to right Y-axis.

splitting cycling (Gokon et al., 2019). Compared with the non-substituted LSM, the production rates of Cu- and Ce-substituted LSM during the CS step rapidly decayed after reaching the peak rate. This leads to a decrease in the amount of CO production compared with the non-substituted LSM (**Figure 3B**). In the case of group B (**Figure 5B**), the order of peak rates of the CO production was Fe-[64.2–65.0 μmol/(min·g-material)] < Ga-[66.8–68.1 μmol/(min·g-material)] < Al-substituted LSMs [74.6–77.5 μmol/(min·g-material)] in second to fourth runs. The time required for CO production in the Al- and Ga-substituted LSMs was extended to approximately 25 min. These results correspond to the results that the Al- and Ga-substituted LSMs enhanced CO production during the CS step (**Figure 3B**). For the group C (**Figure 5C**), the peak rates of the CO production were Co-[65.6–66.5 μmol/(min·g-material)], Mg-[74.2–75.6 μmol/(min·g-material)], and Ni-substituted LSMs [72.9–76.1 μmol/(min·g-material)] in the second to fourth runs (Co < Mg ≅ Ni). The period of time for CO production in group C was extended to approximately 30 min. These results of increased peak rate and prolonged CO production lead to an increase in the amount of CO production in group C compared to the non-substituted LSM.

In this section, all samples of substituted and non-substituted LSMs were compared in terms of redox activity and reaction kinetics under the same test conditions. In particular, Mg-, Co-, and Ni-substituted LSMs in group C demonstrated higher CO productivity and superior reaction kinetics than the non-substituted LSM.

Temperature Impacts of the TR and CS Steps on Redox Activity of Mg-, Co-, and Ni-Substituted LSMs

In this section, in order to examine the effect of temperature on the redox activity of substituted LSMs in group C, the samples were subjected to the TR step at a temperature of 1,200°C for 90 min. Subsequently, the CS step was performed at temperatures of 800°C–1,200°C for 30 min (**Figure 6A**). As shown in **Figure 6B**, the TR step was conducted at temperatures of 1,200°C–1,400°C for 90 min, and subsequently the CS step was performed at a temperature of 1,200°C for 30 min. The TGA profiles of Mg-, Co-, Ni-substituted LSMs were displayed in **Supplementary Figure S3**. As seen in **Figure 6A**, Average O_2 productivity at TR temperature of 1,400°C were approximately similar at 183.7 μmol/(min·g-material) (standard deviation (SD) = 0.26) for Mg-substituted LSM, and 183.4 μmol/(min·g-material) (SD = 5.19) for Co-substituted LSM, while 194.5 μmol/(min·g-material) (SD = 2.79) for Ni-substituted LSM was highest among the group C. Even if the CS temperature decreased from 1,200°C to 800°C, the average CO productivity at CS temperature of 800°C–1,200°C were 344.4 μmol/(min·g-material) (SD = 5.63) for Mg-substituted LSM, 347.1 μmol/(min·g-material) (SD = 15.84) for Co-substituted LSM, and 349.7 μmol/(min·g-material) (SD = 5.61) for Ni-substituted LSM. The temperatures in the exothermic CS step did not influence CO productivity in the present test conditions. However, the peak rate of CO production

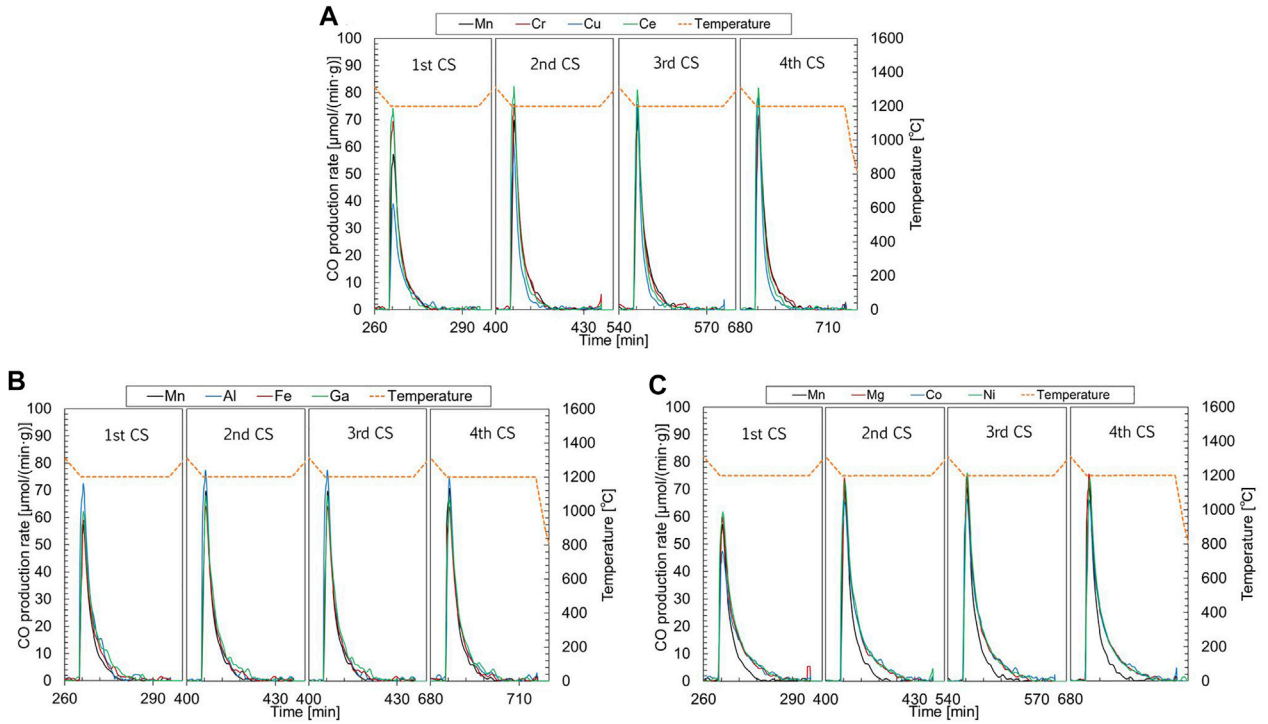

FIGURE 5 | CO production profiles of samples belonging to **(A)** group A (Cu, Cr, and Ce-substituted LSMs), **(B)** group B (Fe, Al, and Ga-substituted LSMs), and **(C)** group C (Co, Ni and Mg-substituted LSMs) during the TR step in the first to fourth runs. The production profiles correspond to left Y-axis, while the temperature profile corresponds to right Y-axis.

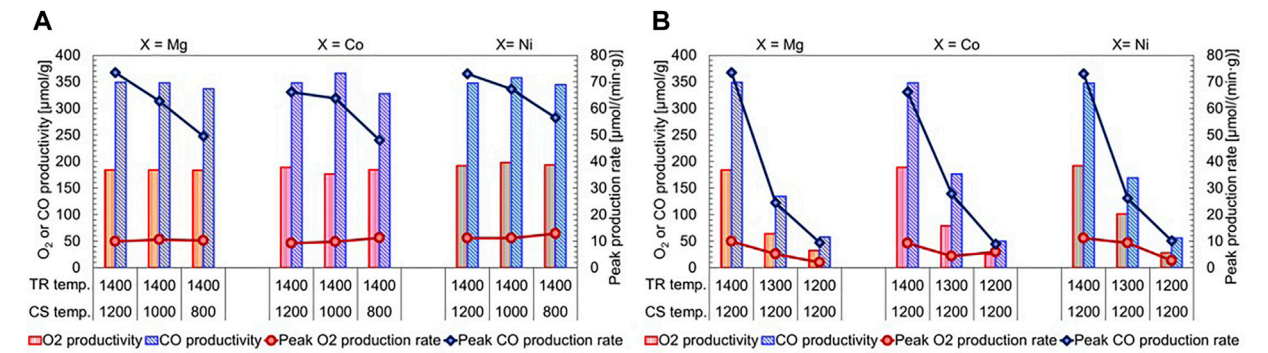

FIGURE 6 | Effects of **(A)** CS and **(B)** TR temperatures on the redox activity of substituted LSMs in group C. **(A)** the samples were subjected to the TR step at a temperature of 1,200°C for 90 min, and the subsequent CS step was performed at temperatures of 800°C–1,200°C for 30 min **(B)** the TR step was conducted at temperatures of 1,200°C–1,400°C for 90 min, and subsequently the CS step was performed at a temperature of 1,200°C for 30 min. Each temperature of TR and subsequent CS step shows in below the figure. The O_2 and CO productivities correspond to left Y-axis, while the peak rates of production correspond to right Y-axis.

decreased as the CS temperature decreased. Thus, the results indicate that the CS temperature contributes to the oxidation kinetics of the reduced sample during the CS step. The average CO/O_2 ratios and test conditions are 1.79–2.10, 1.84–2.24, 1.67–2.00 for the Mg-, Co-, and Ni-substituted LSMs, respectively. On average, the stoichiometric CO/O_2 ratio was approximately attained for the samples in group C, meaning that the two-step reaction proceeds stoichiometrically under test conditions of different CS temperatures in **Figure 6A**. The impact of the TR temperature on the redox activity is shown in **Figure 6B**. As the TR temperature decreased from 1,400°C to 1,200°C, the productivities and peak rates of O_2 and CO decreased. The average CO/O_2 ratios were nearly equal to 2.0 for all samples in group C. These results indicate that the samples

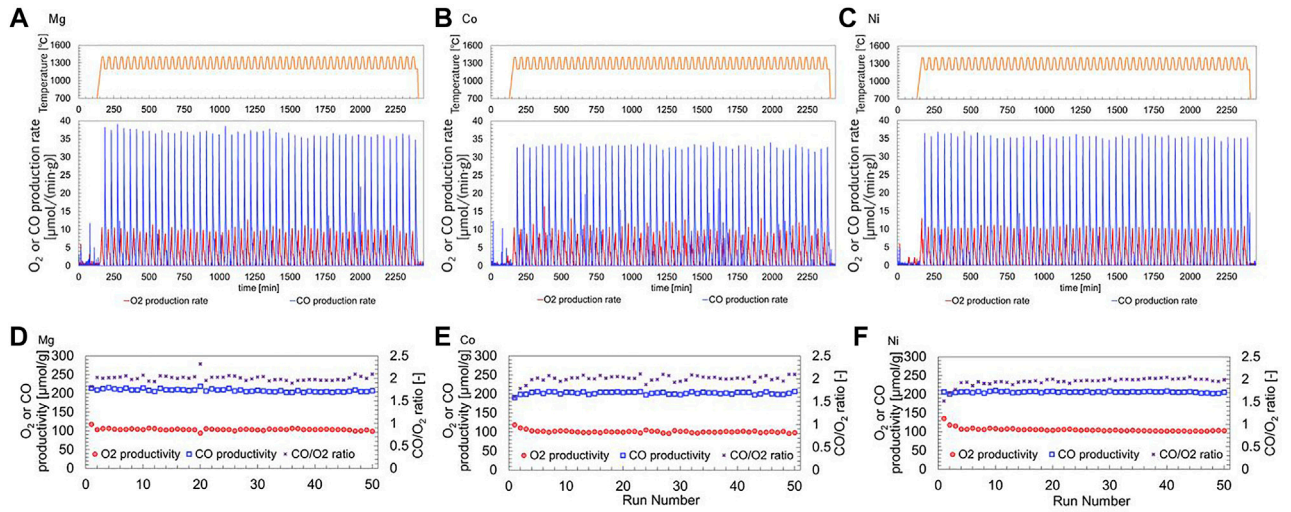

FIGURE 7 | Thermal durability and stability of redox materials for long-term thermochemical cycling. Temperature, O_2 and CO production profiles of **(A)** Mg-, **(B)** Co, **(C)** Ni-substituted LSMs, and O_2 and CO productivities and CO/O_2 ratios of **(D)** Mg-, **(E)** Co, **(F)** Ni-substituted LSMs. The O_2 and CO productivities correspond to left Y-axis, while the O_2/CO ratio of each production correspond to right Y-axis.

maintained stoichiometric two-step reactions under different TR temperatures. Thus, the temperatures in the endothermic TR step strongly affect the redox activity and reaction kinetics in terms of thermodynamics and kinetics for both steps of thermochemical cycling.

The effects of temperature on the redox activity of substituted LSMs in group C were studied in this section; whereby we elucidated that, the TR temperature of 1,400°C and subsequent CS temperatures of 800°C–1,200°C provided large O_2 and CO productivity and reaction rates without degradation of the sample, while the stoichiometric redox activity and reproducible reaction rate were maintained during the repeated test runs. In the following section, the thermal durability and stability of the samples in group C during thermochemical two-step cycling under severe test conditions are examined and evaluated.

Thermal Durability and Stability of Mg, Co, and Ni-Substituted LSMs in Continuous Multiple Cycling of Thermochemical Two-Step Reaction

To prevent the decrease in the reactivity of the redox material owing to sintering and coagulation at high temperatures, the presence of thermal durability and stability of redox materials for thermochemical two-step CO_2 splitting is necessary (Jiang et al., 2014b; Wang et al., 2020; Liu et al., 2021). In the previous section, the highest reactivity and CO production rate were observed in the redox cycles of Mg-, Co-, and Ni-substituted LSMs at TR and CS temperatures of 1,400°C and 1,200°C, respectively, while such high-temperature conditions may cause coagulation and sintering of the sample. Therefore, long-term continuous multiple cycling of the thermochemical two-step reaction was performed to evaluate the thermal durability of the samples. The TR step was performed at 1,400°C for 10 min, and the reduced sample was subjected to a subsequent CS step at 1,200°C for 15 min. The as-synthesized sample before testing and the sample obtained after cycling were observed by SEM to evaluate the thermal stability of the sample at high temperature.

Figure 7A illustrates the thermogravimetric measurements of the continuous TR-CS cycling of thermochemical CO_2 splitting using the Mg-substituted LSM for long-term thermal durability. The profiles of O_2 and CO production were reproducibly observed at the same level without degradation during continuous 50 runs. Similarly, the Co- and Ni-substituted LSMs exhibited stable and reproducible profiles of O_2 and CO production over long-term continuous multiple cycling (**Figures 7B,C**). The O_2 and CO productivity at each run are plotted against the run number in **Figure 7D**. The average values of O_2 and CO productivities were 103.7 (SD = 2.19), and 208.3 (SD = 3.76), respectively. The decreases in O_2 and CO productivity were 4.3% and 1.0% after the 50th run when the standard point for comparison was the second run because the result in the first run might include non-reproducible effects of sample and TGA reactor preparations (moisture and air adsorbed on the surface of sample powder, and contamination in the TGA reactor). The slight decreases in the productivities indicate the two following possibilities: 1) limited spillage of the power-shaped sample together with a releasing/accompanying gas flow and 2) low vaporization of the sample during the repeated runs. However, significant effusion and vaporization of the sample were absent during the continuous runs. The results indicated that the Mg-substituted LSM was a durable and reproducible redox material during long-term thermochemical cycling at high temperatures. As seen in **Figures 7E,F**, stable and reproducible O_2 and CO productivity over the long-term continuous multiple cycling were observed with the remaining stoichiometric ratio of $CO/O_2 \cong 2$ without degradation of redox activity for the Co- and Ni-substituted LSMs, as well as the Mg-substituted LSM.

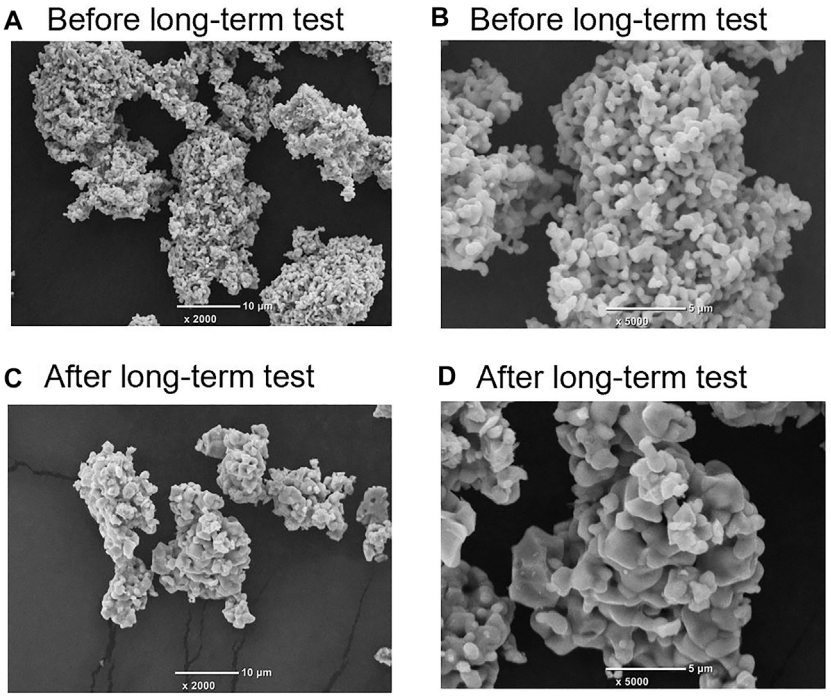

FIGURE 8 | Secondary electron image (SEI) micrograph of the Mg-substituted LSM. The initial sample (before testing) magnification of **(A)** 2,000 and **(B)** 5,000; the sample obtained after the long-term tests magnification of **(C)** 2,000 and **(D)** 5,000.

Figure 8 illustrates the secondary electron image (SEI) micrograph of the Mg-substituted LSM as follows: the initial sample (before testing) magnification of 1) 2,000 and 2) 5,000; after the long-term tests magnification of 3) 2,000 and 4) 5,000. A micrograph of the Co- and Ni-substituted LSMs is shown in **Supplementary Figures S4, S5**. As seen in the initial sample (**Figures 8A,B**), the size of particle was in the range of 0.1–0.5 μm, and non-porous and polygon-shaped particle were numerously observed. After the long-term test (**Figures 8C,D**), a large number of larger particle size 1–3 μm without variation in particle shape appeared in the SEI image. In addition, the particles appear to have coalesced as per the large particle size after the tests. The results indicated that the initial powder sample was partially sintered at high temperatures during long-term tests. However, as shown in **Figure 7D**, the redox performances of the production rate and productivities of O_2 and CO were maintained without degradation during the long-term test. Thus, the results indicate that over a long reaction time, the Mg-substituted LSM retains thermal stability and stable redox performance.

To evaluate the structural stability of the Mg-substituted LSM, we compared the XRD patterns of the samples before and after the long-term test, as shown in **Supplementary Figure S6**. As shown in **Supplementary Figure S6A**, all diffraction peaks assigned to the $La_{0.7}Sr_{0.3}Mn_{0.85}Mg_{0.15}O_3$ reference phase (red vertical bars below the XRD pattern) (Troyanchuk et al., 2015) were indexed in a trigonal unit cell [space group R- 3C (167)], for which the lattice parameters are listed in **Table 2**. The results indicate that the sample was synthesized as a single phase before the test. The diffraction pattern of the sample obtained after the test did not vary. However, a series of peaks resulting from the Si reference phase (Dutta, 1962) (green vertical bars below the XRD pattern) were observed together with the $La_{0.7}Sr_{0.3}Mn_{0.85}Mg_{0.15}O_3$ phase. This is owing to the sample holder made of glass for XRD measurements; no secondary phase occurred in the test. The XRD patterns of Co-, and Ni-substituted LSMs after the long-term test are displayed in **Supplementary Figures S6B,C**, respectively. No secondary phase was also observed in the patterns of both samples as well as the Mg-substituted LSM, although the XRD peaks derived from Si appeared. These results indicate that these substituted LSMs promoted the redox reaction without crystallographic dissociation during the long-term multi-cycling test.

XPS Analysis of Mg-Substituted LSM

The Mg-substituted LSM, which has the highest activity and long-term thermal stability among the LSM perovskites tested in the present study, was selected as a tentative redox material. The change in the valence state of all ionic species was examined for the synthesized sample, and samples obtained after the TR and subsequent CS steps of thermochemical two-step CO_2 splitting by XPS analysis.

Figure 9 shows the La $3d_{5/2}$ and La $3d_{3/2}$ x-ray photoelectron spectra with peak deconvolutions of the synthesized, reduced, and the oxidized samples. As seen in **Figure 9A**, the triplet peaks centered at 833.7, 835.7, and 837.9 eV for the synthesized sample can be assigned to the La $3d_{5/2}$ main peak and La $3d_{5/2}$ satellite

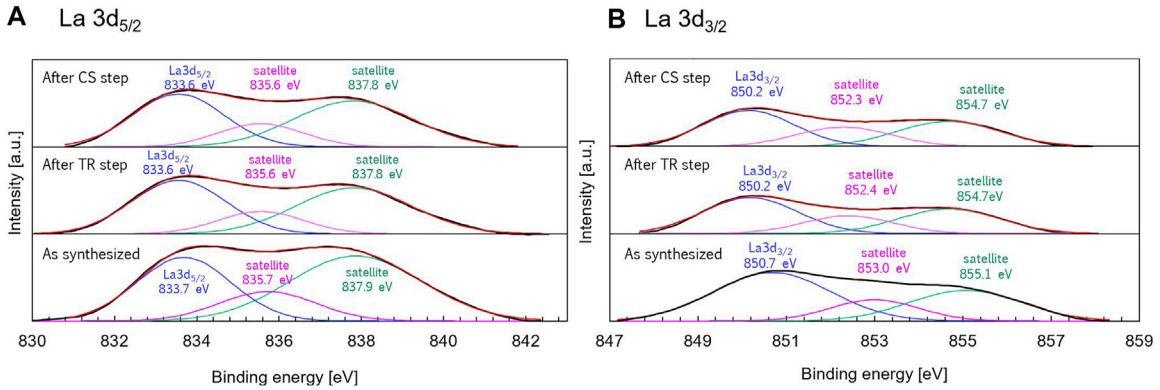

FIGURE 9 | (A) La $3d_{5/2}$ and **(B)** La $3d_{5/2}$ x-ray photoelectron spectra with peak deconvolutions of the synthesized sample (as-prepared sample), thermally-reduced sample obtained after the TR step, and the oxidized sample obtained after the CS step.

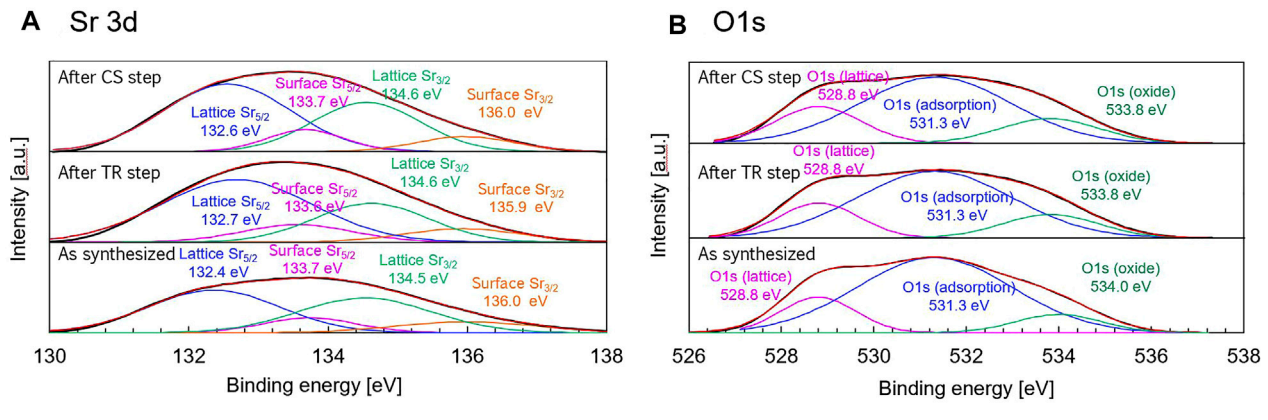

FIGURE 10 | (A) Sr 3d and **(B)** O 1s x-ray photoelectron spectra with peak deconvolutions of the synthesized sample (as-prepared sample), thermally-reduced sample obtained after the TR step, and the oxidized sample obtained after the CS step.

peaks. The binding energies of La $3d_{3/2}$ were located at 850.7 (main peak), 853.0 (satellite peak), and 855.1 eV (satellite peak), as shown in **Figure 9B**. The triplet peaks of La $3d_{5/2}$ and La $3d_{3/2}$ was observed for $LaFe_xO_{3-\delta}$ perovskites with different x values ($0.7 \leq x \leq 1.3$) in the previous work. The satellite peaks could be assigned to the antibonding and bonding components of the 3d state (Cao et al., 2016). These data of the present study indicate that lanthanum ions are present in the trivalent form for the synthesized sample. Negligible differences were observed in terms of the binding energies of the synthesized, reduced, and the oxidized samples, indicating that the valence state of La did not change during the thermochemical process.

The results of XPS analysis for Sr 3d and O 1s spectra with peak deconvolutions are shown in **Figure 10**. As shown in **Figure 10A**, the Sr 3d spectrum of the synthesized sample was fitted into two doublets (Sr $3d_{5/2}$ and Sr $3d_{3/2}$). The doublet peaks of Sr $3d_{5/2}$ were centered at 132.4 (main peak) and 133.7 eV (satellite peak), while those of Sr $3d_{3/2}$ were located at 134.5 (main peak) and 136.0 eV (satellite peak). The peaks of Sr 3d and O 1s were divided into two components resulting from the surface and lattice (Wang et al., 2017). The high binding energy component of Sr $3d_{3/2}$ corresponds to the position of Sr $3d_{3/2}$ in SrO segregated on the surface, while the low binding energy component of the Sr $3d_{3/2}$ can be attributed to Sr in the manganite structure (Bertacco et al., 2002). The binding energy of Sr $3d_{5/2}$ was approximately 2.1 eV higher than that of Sr $3d_{3/2}$. The peak of Sr $3d_{5/2}$ located in low-binding energy region (131.6–132.7 eV) is regarded as lattice component owing to the perovskite structure on the near-surface region, on the other hand, that located in high-binding energy region (133.4–133.6 eV) is considered as component of surface termination (strontium oxide/strontium hydroxide/strontium carbonate) (Wang et al., 2017). The peak area in the lattice component of Sr $3d_{5/2}$ for the synthesized, reduced, and oxidized samples are 4.0, 4.9, and 5.1 times as much as that of the surface component. The Sr 3d data of the present study indicate that Sr resulting from the lattice component is more dominant than the surface termination component, and the binding energies of all components for the synthesized, reduced, and oxidized samples exhibit negligible variation. Thus, the valence state of Sr varies negligibly during the thermochemical process.

TABLE 3 | Mn valence v_{Mn} for the synthesized sample (as-prepared sample), thermally-reduced sample obtained after the TR step, and the oxidized sample obtained after the CS step. The values were estimated from Mn 3s, and Mn 2p x-ray photoelectron spectra.

Sample	Mn 3s				Mn 2p			O1s			
	peak position E1 (eV)	peak position E2 (eV)	ΔE (eV)	valence states of Mn	Mn3+ peak area (eV)	Mn4+ peak area (eV)	Mn3+/ Mn4+	lattice peak area sI (eV)	adsorptive peak area sII (eV)	oxide peak area sIII (eV)	Lattice peak ratio Rlattice (%)
After CS step	83.046	87.987	4.94	3.39	3689	1095	3.37	3081	9904	2377	56.4
After TR step	83.209	88.405	5.20	3.07	3685	1105	3.33	2784	10293	2240	55.4
As synthesized	82.884	88.005	5.12	3.2	4009	1223	3.28	2652	11619	1565	62.9

The Sr 3d data can be related to the results of O 1s data by separating the spectrum into two components: lattice and surface. The O 1s spectra with peak deconvolution are shown in **Figure 10B**. There are three types of oxygen: O_I (528.8 eV), O_{II} (531.3 eV), and O_{III} (534.0 eV), which represent the lattice oxygen, adsorbed O_2^{2-}/O^-, and oxide (or secondary phase). In the O 1s data, the lattice O_I and surface O_{II} do not vary in the binding energies of the synthesized, reduced, and oxidized samples, while the surface O_{III} does not change after the thermochemical process of the TR and CS steps. The area ratios of $O_I/(O_{II} + O_{III})$ in the O 1s data are 0.20, 0.22, and 0.25 for the synthesized, reduced, and oxidized samples, respectively. The results indicate that the oxygen resulting from the adsorbed and secondary phase area is predominant in the surface area relative to the oxygen corresponding to the lattice component. The O 1s located at 528.8 eV in the low-binding-energy region (528.7–529.7 eV) corresponds to lattice oxygen in the structure of perovskite oxide (McIntyre and Cook, 1975; Vasquez, 1991; Galenda et al., 2007; Wang et al., 2016). The peak of O 1s located at 531.3 eV in high-binding energy region (531.1–531.6 eV) is regarded as a component of surface termination resulting from an adsorbed oxygen and carbonate phase (McIntyre and Cook, 1975; Uwamino et al., 1984; Norman and Leach, 2011; Wang et al., 2016). The peaks of O 1s located at 533.8–534.0 eV are considered an oxygen component of adsorbed OH^- or absorbed bulk oxygen species and metal oxide (Sakairi et al., 2015). The O_{III} (534.0 eV) could be related to the presence of the $Mg(OH)_2$ species (Yao et al., 2000). Peak areas of lattice oxygen (s_I), adsorptive species (s_{II}), and surface oxygen (s_{III}) in O 1s spectra were listed in **Table 3**. A lattice peak ratio ($R_{lattice}$) was calculated using s_I and s_{III} data.

$$R_{lattice} = (s_I + s_{III})$$

The value for $R_{lattice}$ decreased after the TR step, and increased after the subsequent CS step. This change of $R_{lattice}$ was in good agreement with the weight change obtained by thermochemical redox cycle with TGA.

The Mn 3s, Mn 2p, and Mg 2p spectra with peak deconvolutions are shown in **Figure 11**. As seen in **Figure 11A**, the Mn 3s spectrum for the synthesized sample fitted doublet peaks are centered at 82.9 and 88.0 eV. The peak centered at 92.2 eV may correspond to La 4d satellite signals (Galakhov et al., 2002). It was reported that the magnitude of the Mn 3s splitting decreases monotonically with an increase in the formal valence of the manganese ions (Galakhov et al., 2002). The Mn valence, v_{Mn} (eV) was estimated using the following linear equation:

$$v_{Mn} = 9.67 - 1.27\Delta E_{Mn3s}$$

where ΔE_{Mn3s} is the difference in binding energy between the Mn 3s doublet (Beyreuther et al., 2006). The linear relationship between v_{Mn} and ΔE_{Mn3s} was derived for the valence range between +2 and +4 from XPS investigations of different bulk mixed-valent manganites and binary Mn oxides, respectively. The results of the Mn valence v_{Mn} for the synthesized, reduced, and oxidized samples are listed in **Table 3**; for which the values of ΔE_{Mn3s} were 5.12, 5.20, and 4.94 eV, respectively. The corresponding valence states of Mn are 3.20, 3.07, and 3.39, respectively. The Mn valence v_{Mn} decreased after the TR step, releasing oxygen, and backwards increased after the subsequent CS step. The results based on Mn 3s spectra indicate that the valence states of Mn ions contribute to the redox reaction in the Mg-substituted LSM during the thermochemical two-step process.

According to previous research (Zhang et al., 2014; Ilango et al., 2016; Xia et al., 2021), the Mn valence in perovskites can also be estimated from the Mn 2p spectra. The Mn 2p spectra with peak deconvolution are shown in **Figure 11B**. For the synthesized sample, the doublet peaks centered at 641.6 and 653.2 eV corresponds to Mn $2p_{3/2}$ and Mn $2p_{5/2}$ of Mn^{3+}, respectively, while the peaks at 644.1 and 656.1 eV represents Mn $2p_{3/2}$ and Mn $2p_{5/2}$ of Mn^{4+}, respectively. According to the peak areas of the Mn^{3+} and Mn^{4+} curves, the corresponding Mn valences can be calculated; the results are shown in **Table 3**. The ratios of Mn^{3+}/Mn^{4+} of the synthesized, reduced, and oxidized samples were 3.28, 3.33, and 3.37 for the as-synthesized samples, after oxygen release, and after CO_2 splitting, respectively. The variations in the Mn valence ratio calculated from the Mn 2p spectra could not describe the redox reaction in the thermochemical two-step process. This is owing to some

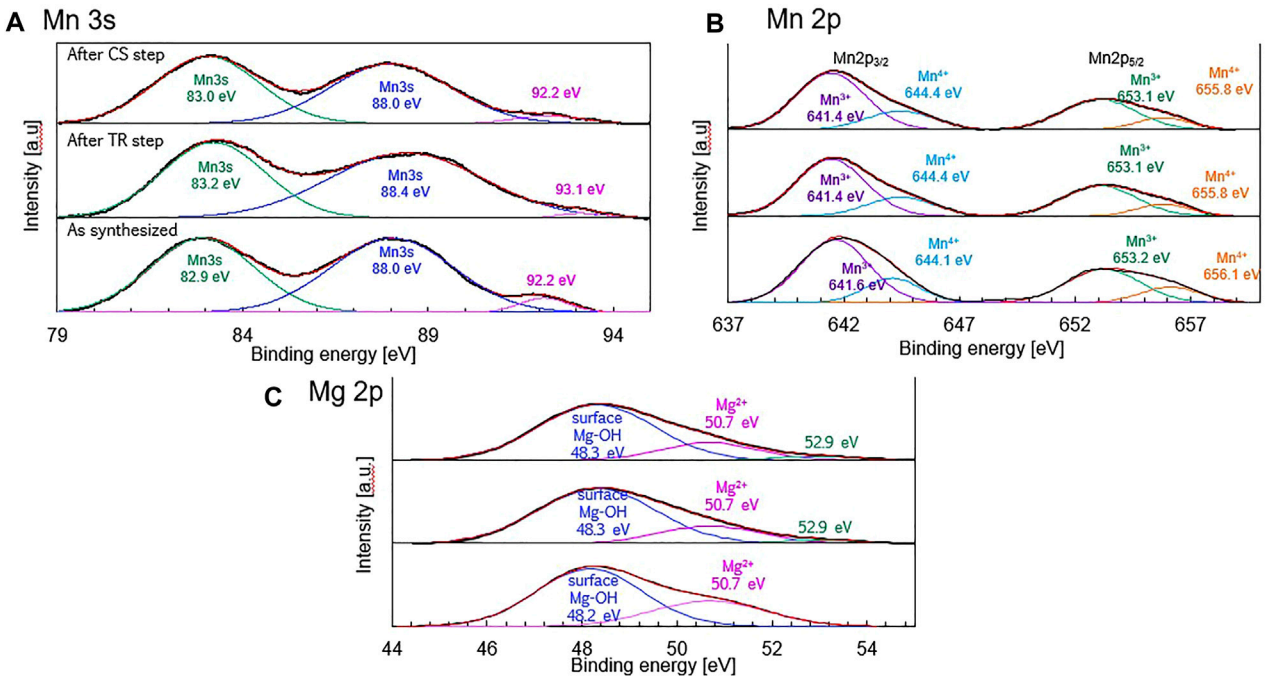

FIGURE 11 | (A) Mn 3s, **(B)** Mn 2p, and **(C)** Mg 2p x-ray photoelectron spectra with peak deconvolutions of the synthesized sample (as-prepared sample), thermally-reduced sample obtained after the TR step, and the oxidized sample obtained after the CS step.

valence states of Mn ions in the Mn 2p spectra in order to superimpose them in the limited binding energies of 640.0–645.0 eV. It is known that the doublet of the Mn 2p spectra cannot specifically distinguish and separate Mn^{2+}/Mn^{3+}/Mn^{4+}, indicating that complicates the estimation of the valence states of Mn (Biesinger et al., 2011; Polfus et al., 2015). According to the results in **Table 3**, the change of $R_{lattice}$ was in good agreement with the results of Mn 3s spectra. Thus, in order to evaluate the variations in Mn valence during the thermochemical two-step process, we considered a secure result based on Mn 3s spectra to estimate the variations in Mn valence.

Figure 11C shows the Mg 2p spectra with peak deconvolution. For the synthesized sample, the binding energies of 48.2 and 50.7 eV correspond to $Mg(OH)_2$ and Mg^{2+}, respectively. Previous studies reported that the binding energies of $Mg(OH)_2$ and MgO were centered at 48.8 and 50.2 eV (Luo et al., 2015), and that of Mg^{2+} and metal Mg were centered at 51.0 and 49.7 eV (Yao et al., 2000). Thus, Mg ions in the Mg-substituted LSM adsorbed hydroxyl groups on the surface of perovskite and existed in the lattice of the crystal structure, indicating that Mg ions are in a bivalent state without metal (zero-valent) in the synthesized sample. Negligible differences (48.2–48.3 eV for $Mg(OH)_2$, 50.7 eV for Mg^{2+}, respectively, were observed in the binding energies of the synthesized, reduced, and oxidized samples, indicating that the valence state of Mg did not vary during the thermochemical process. Therefore, Mg substitution in LSM perovskite enhances the amount of O_2 released and improves fuel production in order to induce variations in the Mn valence without changing the Mg valence during the thermochemical two-step process.

Comparison of Mg, Ni, and Co-Substituted LSMs With Previous Literatures

In the present study, in order to compare the redox reactivity of Mg, Ni, and Co-substituted LSMs the authors selected some literatures with regard to thermochemical two-step CO_2 splitting using LSM perovskites among the numerous previous reports. The main results and test conditions used in previous studies are listed in **Table 4**. It is necessary to be careful for the test equipment and test conditions (reaction time and temperature in both steps) when the results are compared. Thermogravimetric analysis (TGA) indirectly estimates the O_2 and CO productivities from the weight change of the sample during the thermochemical two-step CO_2 splitting cycle. Because the results may include physical gas adsorption/desorption on the surface of the sample, the TGA test may overestimate the productivities in comparison to some reactors (fixed bed, stagnation flow reactor et al.) directly measured O_2 and CO gases using gas chromatography and gas analysis. The test temperatures of the TR and CS steps and the reaction time strongly affected the O_2 and CO productivities. $La_{0.5}Sr_{0.5}Mn_{0.95}Sc_{0.05}O_3$, $La_{0.5}Sr_{0.5}Mn_{0.75}Ga_{0.25}O_3$, and $La_{0.6}Sr_{0.4}MnO_3$ were reported to have high CO productivities (506, 460, and 469 μmol/g-material, respectively) by TGA (Dey et al., 2016; Luciani et al., 2018). There are two possibilities for $La_{0.5}Sr_{0.5}Mn_{0.95}Sc_{0.05}O_3$ and $La_{0.5}Sr_{0.5}Mn_{0.75}Ga_{0.25}O_3$: 1) a reaction time period of 45 min during the CS step. This may

TABLE 4 | Comparison of main results in the present study and previous literatures for thermochemical two-step CO_2 splitting using the LSM perovskites.

Materials	Synthesis method	Reaction equipment	Run number	TR duration (min)	TR temp. (°C)	Average O2 productivity (μmol/g-material)	Average CO productivity (μmol/g-material)	CS duration (min)	CS temp. (°C)	References
La0.7Sr0.3Mn0.9Mg0.1O3	Pechini	TGA	3*	90	1,400	197	354	30	1,200	This work
La0.7Sr0.3Mn0.9Ni0.1O3	Pechini	TGA	3*	90	1,400	188	351	30	1,200	This work
La0.7Sr0.3Mn0.9Co0.1O3	Pechini	TGA	3*	90	1,400	184	347	30	1,200	This work
La0.7Sr0.3MnO3	Pechini	TGA	3*	90	1,400	143	248	30	1,200	This work
La0.5Sr0.5Mn0.95Sc0.05O3	Pechini	TGA	3	45	1,400	323	506	45	1,100	Dey et al. (2016)
La0.5Sr0.5Mn0.75Ga0.25O3	Pechini	TGA	3	45	1,400	264	460	45	1,100	Dey et al. (2016)
La0.5Sr0.5Mn0.9Mg0.1O3	Pechini	TGA	2	45	1,400	190	215	60	1,050	Jouannaux et al. (2019)
La0.65Sr0.35MnO3	Solid-state	TGA	2	45	1,400	100	194	60	1,050	Nair and Abanades, (2018)
La0.5Sr0.5MnO3	Solid-state	TGA	2	45	1,400	195	242	60	1,050	Nair and Abanades, (2018)
La0.6Sr0.4Mn0.5Co0.5O3	Solid-state	TGA	2	45	1,300	315	139	45	1,050	Nair and Abanades, (2018)
LaMn0.5Ni0.5O3	Solid-state	TGA	2	45	1,400	57	105	45	1,050	Nair and Abanades, (2018)
La0.7Sr0.3Mn0.9Cr0.1O3	Pechini	fixed bed	3	30	1,350	98	215	50	1,200	Gokon et al. (2019)
LaCo0.7Zr0.3O3	Pechini	TGA	3	20	1,300	314	224	60	800	Wang et al. (2020)
La0.7Sr0.3MnO3	Solution combustion	TGA	9*	60	1,400	124	209	30	1,000	Takalkar et al. (2021)
La0.6Sr0.4MnO3	Solution combustion	TGA	9*	60	1,400	215	295	30	1,000	Takalkar et al. (2021)
La0.3Sr0.7MnO3	Solution combustion	TGA	9*	60	1,400	188	342	30	1,000	Takalkar et al. (2021)
La0.6Sr0.4FeO3	Pechini sol–gel	TGA	1	20	1,350	427	251	50	1,000	Luciani et al. (2018)
La0.6Sr0.4MnO3	Pechini sol–gel	TGA	1	20	1,350	349	469	50	1,000	Luciani et al. (2018)
La0.6Sr0.4Mn0.8Fe0.2O3	Pechini sol–gel	TGA	1	20	1,350	286	330	50	1,000	Luciani et al. (2018)
La0.6Sr0.4Cr0.8Co0.2O3	Pechini	TGA	3	40	1,200	-	157	40	800	Bork et al. (2015)
La0.5Sr0.5Mn0.83Mg0.17O3	Solid-state	TGA	2	45	1,400	170	208	60	1,050	Demont and Abanades, (2015)
La0.5Sr0.5Mn0.75Al0.25O3	Solid-state	TGA	2	45	1,400	194	221	60	1,050	Demont and Abanades, (2015)
La0.6Sr0.4Mn0.6Al0.4O3	Pechini	Stagnation flow reactor	1	-	1,350	-	294	-	1,000	McDaniel et al. (2013)

lead to enhanced CO productivity owing to slow kinetics of the oxidation reaction for the reduced LSM perovskite, if the kinetics predominate as a rate-determining step in the entire process; 2) a small amount of B site substitution into LSM perovskites may enhance O_2 and CO productivities owing to an improvement of thermal stability under reductive and oxidative atmospheres during the thermochemical processes. However, the data for $La_{0.6}Sr_{0.4}MnO_3$ (Luciani et al., 2018) may be overestimated because O_2 and CO productivities were considerably high in comparison to the productivity levels of O_2 100–215 and CO 194–295 μmol/g-material with similar compositions of LSM perovskites (Nair and Abanades, 2018; Takalkar et al., 2021).

To evaluate the small amount of substitution at the B-site of the LSM perovskite among the previous data, we compared the data between $La_{0.5}Sr_{0.5}Mn_{0.9}Mg_{0.1}O_3$ and $La_{0.5}Sr_{0.5}MnO_3$ (Demont and Abanades, 2015; Jouannaux et al., 2019).

Although the thermochemical cycle was performed under similar test conditions, 10% Mg substitution decreased O_2 productivity and increased CO productivity. On the other hand, the data for $La_{0.7}Sr_{0.3}MnO_3$ in the present study were in the middle level of O_2 and CO productivities and were in good agreement with the previous data listed in **Table 4**. Furthermore, the substitution of 10% Mg, Ni, and Co into the LSM perovskite enhanced O_2 and CO productivities by approximately 1.3–1.4 times. The results indicate that the evaluation of the redox reactivity of the thermochemical cycle is required such that they can be systematically examined using the same test equipment and conditions.

SUMMARY

All samples of substituted and non-substituted LSMs were compared in terms of redox activity and reaction kinetics under the same test conditions. Mg, Ni, and Co-substituted LSM perovskite oxides were proposed for the thermochemical two-step CO_2 splitting process to produce solar fuel. Mg-, Ni-, and Co-substituted LSMs were successfully synthesized as a solid solution of the perovskite structure in a trigonal unit cell without impurities by modified Pechini. In comparison to the non-substituted LSM, the Co, Ni, and Mg substitutions at the B-site of LSM enhanced both O_2 production during the TR step and CO production during the subsequent CS step. The CO/O_2 ratio under the appropriate test conditions was 1.98 (Co-substitution, TR temperature of 1,200°C and CS temperature of 1,200°C), 2.00 (Ni-substitution, TR temperature of 1,200°C and CS temperature of 1,200°C), and 1.90 (Mg-substitution, TR temperature of 1,400°C and CS temperature of 1,200°C), meaning the thermochemical cycling proceeds at approximately the stoichiometric ratio. The peak rates of Co-, Ni-, and Mg-substituted LSMs were the highest among the samples tested in this study. The peak rates of group C were 1.4–1.6 times greater than those of non-substituted LSM. Thus, the Mg-, Co-, and Ni-substituted LSMs in group C demonstrated higher CO productivity and superior reaction kinetics than the non-substituted LSM.

The temperature impacts on the redox activity of substituted LSMs in group C were studied at TR temperatures of 1,200°C–1,400°C and CS temperatures of 800°C–1,200°C. The stoichiometric CO/O_2 ratio at an average was approximately attained for the Mg-, Co-, and Ni-substituted LSMs, indicating that the two-step reaction can proceed stoichiometrically under test conditions of different TR and CS temperatures. The temperatures in the endothermic TR step strongly affected the redox activity and reaction kinetics in terms of thermodynamics and kinetics for both steps of thermochemical cycling.

We examined and evaluated the thermal durability and stability of the redox material for thermochemical two-step CO_2 splitting for the Mg-, Co-, and Ni-substituted LSMs in group C. For all samples, reproducible profiles of O_2 and CO production were observed at the same level without degradation during the continuous 50 runs of thermochemical cycling. The O_2 and CO productivity over the long-term continuous multiple cycling were observed with the remaining stoichiometric ratio of $CO/O_2 \cong 2$ without degradation of redox activity for the Co- and Ni-substituted LSMs as well as the Mg-substituted LSM. Thus, the results indicate that the Mg- Co- and Ni-substituted LSMs retained thermal stability and stable redox performance over a long reaction time.

The change in the valence state of all ionic species for the Mg-substituted LSM was examined for the synthesized sample, and the samples obtained after the TR and subsequent CS steps of thermochemical two-step CO_2 splitting by XPS analysis. The valence states of Mn were estimated to be 3.20, 3.07, and 3.39, respectively. The Mn valence ν_{Mn} decreased after the TR step, releasing oxygen, and backwards increased after the subsequent CS step. The XPS analysis based on Mn 3s spectra indicates that the valence states of Mn ions contribute to the redox reaction in the Mg-substituted LSM during the thermochemical two-step process. We did not observe the valance changes of La, Sr, and Mg in the perovskite oxide in each step of the thermochemical two-step reaction.

The redox reactivity of Mg-, Ni-, and Co-substituted LSMs in the present study were compared with numerous previous reports. In comparing results, it is necessary to be careful with regard to the test equipment and test conditions (reaction time and temperature in both steps). The data for $La_{0.7}Sr_{0.3}MnO_3$ in the present study were in the middle level of O_2 and CO productivities and were in good agreement with the previous data listed in **Table 4**. Furthermore, the substitution of 10% Mg, Ni, and Co into the LSM perovskite enhanced O_2 and CO productivities by approximately 1.3–1.4 times. The results indicate that the evaluation of the redox reactivity of the thermochemical cycle is required such that they can be systematically examined using the same test equipment and conditions.

DATA AVAILABILITY STATEMENT

The data presented in the study are deposited in the Crystallography Open Database repository, accession numbers of 300371, 300372, 300373, 300374, 300386, 300387, 300388, 300389, 1521156, and 1532010.

AUTHOR CONTRIBUTIONS

HS contributed to conduct whole experiments and analysis, visualization and writing—original draft and revision; NG contributed to perform conceptualization, methodology, validation, formal analysis, writing—review and editing, supervision, project administration, funding acquisition, and provide software and resource; KH contributed to collaborate XPS analysis and visualization; YI and DY contributed to collaborate investigation.

FUNDING

This research was partially supported by the Ministry of Education, Culture, Sports, Science and Technology, Challenging Research (Exploratory), JSPS KAKENHI (Grant

Number 21K18920), Grant-in-Aid for Scientific Research (B), JSPS KAKENHI (Grant Number 19H02658) and Grant-in-Aid for Scientific Research (C), JSPS KAKENHI (Grant Number 20K05398).

ACKNOWLEDGMENTS

The authors gratefully acknowledge Naoki Ito at ENEOS Corporation for very helpful discussion, technical staff (Katsutoshi Iwafune) at Niigata University for supporting the XRD measurement, technical staff (Takahiro Nomoto) at Niigata University for supporting the SEM measurement.

SUPPLEMENTARY MATERIAL

The Supplementary Material for this article can be found online at: https://www.frontiersin.org/articles/10.3389/fenrg.2022.872959/full#supplementary-material

REFERENCES

Agrafiotis, C., Roeb, M., and Sattler, C. (2015). A Review on Solar Thermal Syngas Production via Redox Pair-Based Water/carbon Dioxide Splitting Thermochemical Cycles. *Renew. Sustain. Energy Rev.* 42, 254–285. doi:10.1016/j.rser.2014.09.039

Bayon, A., de la Calle, A., Ghose, K. K., Page, A., and McNaughton, R. (2020). Experimental, Computational and Thermodynamic Studies in Perovskites Metal Oxides for Thermochemical Fuel Production: A Review. *Int. J. Hydrogen Energy* 45, 12653–12679. doi:10.1016/j.ijhydene.2020.02.126

Bayon, A., de la Calle, A., Stechel, E. B., and Muhich, C. (2022). Operational Limits of Redox Metal Oxides Performing Thermochemical Water Splitting. *Energy Tech.* 10, 2100222. doi:10.1002/ente.202100222

Bertacco, R., Contour, J. P., Barthélemy, A., and Olivier, J. (2002). Evidence for Strontium Segregation in La 0.7 Sr 0.3 MnO 3 Thin Films Grown by Pulsed Laser Deposition: Consequences for Tunnelling Junctions. *Surf. Sci.* 511, 366–372. doi:10.1016/s0039-6028(02)01546-7

Beyreuther, E., Grafström, S., Eng, L. M., Thiele, C., and Dörr, K. (2006). XPS Investigation of Mn Valence in Lanthanum Manganite Thin Films under Variation of Oxygen Content. *Phys. Rev. B* 73, 155425. doi:10.1103/physrevb.73.155425

Bhosale, R. R., and Takalkar, G. D. (2018). Nanostructured Co-precipitated Ce0.9Ln0.1O2 (Ln = La, Pr, Sm, Nd, Gd, Tb, Dy, or Er) for Thermochemical Conversion of CO2. *Ceram. Int.* 44, 16688–16697. doi:10.1016/j.ceramint.2018.06.096

Biesinger, M. C., Payne, B. P., Grosvenor, A. P., Lau, L. W. M., Gerson, A. R., Smart, R. S. C., et al. (2011). Resolving Surface Chemical States in XPS Analysis of First Row Transition Metals, Oxides and Hydroxides: Cr, Mn, Fe, Co and Ni. *Appl. Surf. Sci.* 257, 2717–2730. doi:10.1016/j.apsusc.2010.10.051

Bork, A. H., Kubicek, M., Struzik, M., and Rupp, J. L. M. (2015). Perovskite La0.6Sr0.4Cr1−xCoxO3−δ Solid Solutions for Solar-Thermochemical Fuel Production: Strategies to Lower the Operation Temperature. *J. Mat. Chem. A* 3, 15546–15557. doi:10.1039/c5ta02519b

Bulfin, B., Miranda, M., and Steinfeld, A. (2021). Performance Indicators for Benchmarking Solar Thermochemical Fuel Processes and Reactors. *Front. Energy Res.* 9, 677980. doi:10.3389/fenrg.2021.677980

Cao, K., Cao, E., Zhang, Y., Hao, W., Sun, L., and Peng, H. (2016). The Influence of Nonstoichiometry on Electrical Transport and Ethanol Sensing Characteristics for Nanocrystalline LaFe O3− Sensors. *Sensors Actuators B Chem.* 230, 592–599. doi:10.1016/j.snb.2016.02.096

Chen, Y., Yang, L., Ren, F., and An, K. (2014). Visualizing the Structural Evolution of LSM/*x*YSZ Composite Cathodes for SOFC by *in-situ* Neutron Diffraction. *Sci. Rep.* 4, 5179. doi:10.1038/srep05179

Deml, A. M., Stevanović, V., Holder, A. M., Sanders, M., O'Hayre, R., and Musgrave, C. B. (2014). Tunable Oxygen Vacancy Formation Energetics in the Complex Perovskite Oxide SrxLa1-xMnyAl1-yO3. *Chem. Mat.* 26, 6595–6602. doi:10.1021/cm5033755

Demont, A., Abanades, S., and Beche, E. (2014). Investigation of Perovskite Structures as Oxygen-Exchange Redox Materials for Hydrogen Production from Thermochemical Two-step Water-Splitting Cycles. *J. Phys. Chem. C* 118, 12682–12692. doi:10.1021/jp5034849

Demont, A., and Abanades, S. (2014). High Redox Activity of Sr-Substituted Lanthanum Manganite Perovskites for Two-step Thermochemical Dissociation of CO2. *RSC Adv.* 4, 54885–54891. doi:10.1039/c4ra10578h

Demont, A., and Abanades, S. (2015). Solar Thermochemical Conversion of CO2 into Fuel via Two-step Redox Cycling of Non-stoichiometric Mn-Containing Perovskite Oxides. *J. Mat. Chem. A* 3, 3536–3546. doi:10.1039/c4ta06655c

Dey, S., Naidu, B. S., Govindaraj, A., and Rao, C. N. R. (2015). Noteworthy Performance of La1−xCaxMnO3 Perovskites in Generating H2 and CO by the Thermochemical Splitting of H2O and CO2. *Phys. Chem. Chem. Phys.* 17, 122–125. doi:10.1039/c4cp04578e

Dey, S., Naidu, B. S., and Rao, C. N. R. (2016). Beneficial Effects of Substituting Trivalent Ions in the B-Site of La0.5Sr0.5Mn1−xAxO3 (A = Al, Ga, Sc) on the Thermochemical Generation of CO and H2 from CO2 and H2O. *Dalton Trans.* 45, 2430–2435. doi:10.1039/c5dt04822b

Dey, S., Naidu, B. S., and Rao, C. N. R. (2015). Ln0.5A0.5MnO3(Ln=Lanthanide, A= Ca, Sr) Perovskites Exhibiting Remarkable Performance in the Thermochemical Generation of CO and H2from CO2and H2O. *Chem. Eur. J.* 21, 7077–7081. doi:10.1002/chem.201500442

Dutta, B. N. (1962). Lattice Constants and Thermal Expansion of Silicon up to 900 °C by X-Ray Method. *Phys. Stat. Sol. (b)* 2, 984–987. doi:10.1002/pssb.19620020803

El-Fadli, Z., Redouane Metni, M., Sapiña, F., Martinez, E., José-Vicente Folgado, and, A., and Beltrán, A. (2002). Electronic Properties of Mixed-Valence Manganates: The Role of Mn Substitutional Defects. *Chem. Mat.* 14, 688–696. doi:10.1021/cm010655e

Galakhov, V. R., Demeter, M., Bartkowski, S., Neumann, M., Ovechkina, N. A., Kurmaev, E. Z., et al. (2002). Mn3sexchange Splitting in Mixed-Valence Manganites. *Phys. Rev. B* 65, 113102. doi:10.1103/physrevb.65.113102

Galenda, A., Natile, M. M., Krishnan, V., Bertagnolli, H., and Glisenti, A. (2007). LaSrCoFeO and Fe2O3/LaSrCoFeO Powders: Synthesis and Characterization. *Chem. Mat.* 19, 2796–2808. doi:10.1021/cm062742i

Ginley, D. S., and Cahen, D. (2011). *Fundamentals of Materials for Energy and Environmental Sustainability*. Cambridge University Press.

Gokon, N., Hara, K., Ito, N., Sawaguri, H., Bellan, S., Kodama, T., et al. (2020). Thermochemical H_2O Splitting Using $LaSrMnCrO_3$ of Perovskite Oxides for Solar Hydrogen Production. *AIP Conf. Proc.* 2303, 170007.

Gokon, N., Hara, K., Sugiyama, Y., Bellan, S., Kodama, T., and Hyun-seok, C. (2019). Thermochemical Two-step Water Splitting Cycle Using Perovskite Oxides Based on LaSrMnO3 Redox System for Solar H2 Production. *Thermochim. Acta* 680, 178374. doi:10.1016/j.tca.2019.178374

Gokon, N., Suda, T., and Kodama, T. (2015). Oxygen and Hydrogen Productivities and Repeatable Reactivity of 30-Mol%-Fe-, Co-, Ni-, Mn-Doped $CeO_{2-\delta}$ for Thermochemical Two-step Water-Splitting Cycle. *Energy* 90, 1280–1289.

Hussain, A., Arif, S. M., and Aslam, M. (2017). Emerging Renewable and Sustainable Energy Technologies: State of the Art. *Renew. Sustain. Energy Rev.* 71, 12–28. doi:10.1016/j.rser.2016.12.033

Ilango, P. R., Prasanna, K., Do, S. J., Jo, Y. N., and Lee, C. W. (2016). Eco-friendly Nitrogen-Containing Carbon Encapsulated LiMn2O4 Cathodes to Enhance the Electrochemical Properties in Rechargeable Li-Ion Batteries. *Sci. Rep.* 6, 29826. doi:10.1038/srep29826

Jiang, Q., Tong, J., Zhou, G., Jiang, Z., Li, Z., and Li, C. (2014). Thermochemical CO2 Splitting Reaction with Supported LaxA1−xFeyB1−yO3 (A=Sr, Ce, B=Co, Mn; $0 \leqslant x$, $Y \leqslant 1$) Perovskite Oxides. *Sol. Energy* 103, 425–437. doi:10.1016/j.solener.2014.02.033

Jiang, Q., Zhou, G., Jiang, Z., and Li, C. (2014). Thermochemical CO2 Splitting Reaction with CexM1−xO2−δ (M=Ti4+, Sn4+, Hf4+, Zr4+, La3+, Y3+ and Sm3+) Solid Solutions. *Sol. Energy* 99, 55–66. doi:10.1016/j.solener.2013.10.021

Jouannaux, J., Haeussler, A., Drobek, M., Ayral, A., Abanades, S., and Julbe, A. (2019). Lanthanum Manganite Perovskite Ceramic Powders for CO2 Splitting: Influence of Pechini Synthesis Parameters on Sinterability and Reactivity. *Ceram. Int.* 45, 15636–15648. doi:10.1016/j.ceramint.2019.05.075

Kim, J., Johnson, T. A., Miller, J. E., Stechel, E. B., and Maravelias, C. T. (2012). Fuel Production from CO2 Using Solar-Thermal Energy: System Level Analysis. *Energy Environ. Sci.* 5, 8417–8429. doi:10.1039/c2ee21798h

Lange, M., Roeb, M., Sattler, C., and Pitz-Paal, R. (2014). T-S Diagram Efficiency Analysis of Two-step Thermochemical Cycles for Solar Water Splitting under Various Process Conditions. *Energy* 67, 298–308. doi:10.1016/j.energy.2014.01.112

Liu, X., Wang, T., Gao, K., Meng, X., Song, C., Zhu, Z., et al. (2021). Ca- and Ga-Doped LaMnO3 for Solar Thermochemical CO2 Splitting with High Fuel Yield and Cycle Stability. *ACS Appl. Energy Mat.* 4, 9000–90129012. doi:10.1021/acsaem.1c01274

Lu, Y., Zhu, L., Agrafiotis, C., Vieten, J., Roeb, M., and Sattler, C. (2019). Solar Fuels Production: Two-step Thermochemical Cycles with Cerium-Based Oxides. *Prog. Energy Combust. Sci.* 75, 100785. doi:10.1016/j.pecs.2019.100785

Lubomirsky, I., and Cahen, D. (2012). Energy Limitations on Materials Availability. *MRS Bull.* 37, 412–416. doi:10.1557/mrs.2012.56

Luciani, G., Landi, G., Aronne, A., and Di Benedetto, A. (2018). Partial Substitution of B Cation in La0.6Sr0.4MnO3 Perovskites: A Promising Strategy to Improve the Redox Properties Useful for Solar Thermochemical Water and Carbon Dioxide Splitting. *Sol. Energy* 171, 1–7. doi:10.1016/j.solener.2018.06.058

Luo, Y., Sun, Y., Lv, J., WangWang, X. J., Li, J., and Wang, F. (2015). Transition of Interface Oxide Layer from Porous Mg(OH)2 to Dense MgO Induced by Polyaniline and Corrosion Resistance of Mg Alloy Therefrom. *Appl. Surf. Sci.* 328, 247–254. doi:10.1016/j.apsusc.2014.11.177

Marxer, D., Furler, P., Scheffe, J., Geerlings, H., Falter, C., Batteiger, V., et al. (2015). Demonstration of the Entire Production Chain to Renewable Kerosene via Solar Thermochemical Splitting of H2O and CO2. *Energy fuels.* 29, 3241–3250. doi:10.1021/acs.energyfuels.5b00351

McCabe, E. E., and Greaves, C. (2006). Synthesis and Structural and Magnetic Characterization of Mixed Manganese-Copper N = 1 Ruddlesden-Popper Phases. *Mater. Sci. Eng. B* 98, 5774–5781. doi:10.1016/s0921-5107(02)00758-4

McDaniel, A. H., Miller, E. C., Arifin, D., Ambrosini, A., Coker, E. N., O'Hayre, R., et al. (2013). Sr- and Mn-Doped LaAlO3−δ for Solar Thermochemical H2 and CO Production. *Energy Environ. Sci.* 6, 2424–2428. doi:10.1039/c3ee41372a

McIntyre, N. S., and Cook, M. G. (1975). X-ray Photoelectron Studies on Some Oxides and Hydroxides of Cobalt, Nickel, and Copper. *Anal. Chem.* 47, 2208–2213. doi:10.1021/ac60363a034

Meng, Q.-L., Lee, C.-i., Ishihara, T., Kaneko, H., and Tamaura, Y. (2011). Reactivity of CeO2-Based Ceramics for Solar Hydrogen Production via a Two-step Water-Splitting Cycle with Concentrated Solar Energy. *Int. J. Hydrogen Energy* 36, 13435–13441. doi:10.1016/j.ijhydene.2011.07.089

Miller, J. E., McDaniel, A. H., and Allendorf, M. D. (2014). Considerations in the Design of Materials for Solar-Driven Fuel Production Using Metal-Oxide Thermochemical Cycles. *Adv. Energy Mat.* 4, 1300469. doi:10.1002/aenm.201300469

Mostafa, M. F., Ata-Allah, S. S., and Refai, H. S. (2008). Synthesis, Structure and Electric Studies for La0.7A0.3Mn0.96(InxAl(1−x))0.04O3; A=Ca and Sr Perovskites. *J. Solid State Chem.* 181, 1056–1069. doi:10.1016/j.jssc.2008.01.038

Nair, M. M., and Abanades, S. (2018). Experimental Screening of Perovskite Oxides as Efficient Redox Materials for Solar Thermochemical CO2 Conversion. *Sustain. Energy Fuels* 2, 843–854. doi:10.1039/c7se00516d

Norman, C., and Leach, C. (2011). *In Situ* high Temperature X-Ray Photoelectron Spectroscopy Study of Barium Strontium Iron Cobalt Oxide. *J. Membr. Sci.* 382, 158–165. doi:10.1016/j.memsci.2011.08.006

Orfila, M., Linares, M., Molina, R., Botas, J., Sanz, R., and Marugán, J. (2016). Perovskite Materials for Hydrogen Production by Thermochemical Water Splitting. *Int. J. Hydrogen Energy* 41, 19329–19338. doi:10.1016/j.ijhydene.2016.07.041

Paiva-Santos, C. O., Marques, R. F. C., Jafelicci, M., and Varanda, L. C. (2002). X-ray Powder Data and Bond Valence of La0.65Sr0.35MnO3 after Rietveld Refinement. *Powder Diffr.* 17, 149–152. doi:10.1154/1.1481522

Pechini, M. P. (1967). *U. S. Pat.* 3, 330697.

Petrov, A. N., Voronin, V. I., Norby, T., and Kofstad, P. (1999). Crystal Structure of the Mixed Oxides La0.7Sr0.3Co1−zMnzO3±y(0≤z≤1). *J. Solid State Chem.* 143, 52–57. doi:10.1006/jssc.1998.8073

Polfus, J. M., Xing, W., Sunding, M. F., Hanetho, S. M., Dahl, P. I., Larring, Y., et al. (2015). Doping Strategies for Increased Oxygen Permeability of CaTiO3 Based Membranes. *J. Membr. Sci.* 482, 137–143. doi:10.1016/j.memsci.2015.02.036

Press, W. H., and Teukolsky, S. A. (1990). Savitzky-Golay Smoothing Filters. *Comput. Phys.* 4, 669. doi:10.1063/1.4822961

Randhir, K., Rhodes, N. R., Li, L., AuYeung, N., Hahn, D. W., Mei, R., et al. (2018). Magnesioferrites for Solar Thermochemical Fuel Production. *Sol. Energy* 163, 1–15. doi:10.1016/j.solener.2017.12.006

Reshmi, C. P., Savitha Pillai, S., Suresh, K. G., and Varma, M. R. (2013). Room Temperature Magnetocaloric Properties of Ni Substituted La0.67Sr0.33MnO3. *Solid State Sci.* 19, 130–135. doi:10.1016/j.solidstatesciences.2013.02.019

Riaz, A., Kreider, P., Kremer, F., Tabassum, H., Yeoh, J. S., Lipinski, W., et al. (2019). Electrospun Manganese-Based Perovskites as Efficient Oxygen Exchange Redox Materials for Improved Solar Thermochemical CO_2 Splitting. *ACS Appl. Energy Mater.* 2, 2495–2505. doi:10.1021/acsaem.8b01994

Sakairi, M., Sasaki, R., and Suzuki, K. (2015). Surface Analysis of Al Alloys with X-Ray Photoelectron and Auger Electron Spectroscopies. *Zakaep* 64, 281–284. doi:10.3323/jcorr.64.281

Sawaguri, H., Gokon, N., Cho, H., and Kodama, T. (2021). Selvan Bellan, Temperature Impacts on Reactivity of $La_{0.7}A_{0.3}Mn_{0.9}C_{r0.1}O_{3-\delta}$ of Perovskite Oxides in a Thermochemical Two-step H_2O/CO_2 Splitting. *SolarPACES*. Online, September 27 – October 1, 2021.

Sawaguri, H., Gokon, N., Ito, N., Bellan, S., Kodama, T., and Cho, H. (2020). Thermochemical Two-step CO_2 Splitting Using $La_{0.7}Sr_{0.3}Mn_{0.9}Cr_{0.1}O_3$ of Perovskite Oxide for Solar Fuel Production. *AIP Conf. Proc.* 2303, 170013.

Scheffe, J. R., Weibel, D., and Steinfeld, A. (2013). Lanthanum-Strontium-Manganese Perovskites as Redox Materials for Solar Thermochemical Splitting of H2O and CO2. *Energy fuels.* 27, 4250–4257. doi:10.1021/ef301923h

Schunk, L. O., Haeberling, P., Wepf, S., Wuillemin, D., Meier, A., and Steinfeld, A. (2008). A Receiver-Reactor for the Solar Thermal Dissociation of Zinc Oxide. *J. Sol. Energy Eng.* 2, 130. doi:10.1115/1.2840576

Shannon, R. D., and Prewitt, C. T. (1969). Effective Ionic Radii in Oxides and Fluorides. *Acta Crystallogr. Sect. B* 25, 925–946. doi:10.1107/s0567740869003220

Shirley, D. A. (1972). High-Resolution X-Ray Photoemission Spectrum of the Valence Bands of Gold. *Phys. Rev. B* 5, 4709–4714. doi:10.1103/physrevb.5.4709

Sunarso, J., Hashim, S. S., Zhu, N., and Zhou, W. (2017). Perovskite Oxides Applications in High Temperature Oxygen Separation, Solid Oxide Fuel Cell and Membrane Reactor: A Review. *Prog. Energy Combust. Sci.* 61, 57–77. doi:10.1016/j.pecs.2017.03.003

Takalkar, G., Bhosale, R., and AlMomani, F. (2019). Combustion Synthesized A0.5Sr0.5MnO3-δ Perovskites (Where, A = La, Nd, Sm, Gd, Tb, Pr, Dy, and Y) as Redox Materials for Thermochemical Splitting of CO2. *Appl. Surf. Sci.* 489, 80–91. doi:10.1016/j.apsusc.2019.05.284

Takalkar, G., Bhosale, R. R., AlMomani, F., Kumar, A., Banu, A., Ashok, A., et al. (2020). Thermochemical Splitting of CO2 Using Solution Combustion Synthesized LaMO3 (Where, M = Co, Fe, Mn, Ni, Al, Cr, Sr). *Appl. Surf. Sci.* 509, 144908. doi:10.1016/j.apsusc.2019.144908

Takalkar, G., Bhosale, R. R., AlMomani, F., Rashid, S., Qiblawey, H., Saleh Saad, M. A., et al. (2021). Thermochemical Splitting of CO2 Using Solution Combustion Synthesized Lanthanum-Strontium-Manganese Perovskites. *Fuel* 285, 119154. doi:10.1016/j.fuel.2020.119154

Takalkar, G., and Bhosale, R. R. (2019). Solar Thermocatalytic Conversion of CO2 Using PrxSr(1−x)MnO3−δ Perovskites. *Fuel* 254, 115624. doi:10.1016/j.fuel.2019.115624

Tamaura, Y., Steinfeld, A., Kuhn, P., and Ehrensberger, K. (1995). Production of Solar Hydrogen by a Novel, 2-step, Water-Splitting Thermochemical Cycle. *Energy* 20, 325–330. doi:10.1016/0360-5442(94)00099-o

Troyanchuk, I. O., Bushinsky, M. V., Efimov, V., Schorr, S., Ritter, C., and Sikolenko, V. (2015). Ferromagnetic Ordering in La0.7Sr0.3Mn3+0.85Nb5+0.15O3 Manganite. *Powder Diffr.* 30 (S1), S97–S100. doi:10.1017/s0885715615000032

Uwamino, Y., Ishizuka, T., and Yamatera, H. (1984). X-ray Photoelectron Spectroscopy of Rare-Earth Compounds. *J. Electron Spectrosc. Relat. Phenom.* 34, 67–78. doi:10.1016/0368-2048(84)80060-2

Vasquez, R. P. (1991). X-ray Photoelectron Spectroscopy Study of Sr and Ba Compounds. *J. Electron Spectrosc. Relat. Phenom.* 56, 217–240. doi:10.1016/0368-2048(91)85005-e

Vogt, T., and Schmahl, W. W. (1993). The High-Temperature Phase Transition in Perovskite. *Europhys. Lett.* 24, 281–285. doi:10.1209/0295-5075/24/4/008

Wang, L., Ma, T., Dai, S., Ren, T., Chang, Z., Dou, L., et al. (2020). Experimental Study on the High Performance of Zr Doped LaCoO3 for Solar Thermochemical CO Production. *Chem. Eng. J.* 389, 124426. doi:10.1016/j.cej.2020.124426

Wang, W., Yuan, F., Niu, X., and Zhu, Y. (2016). Preparation of Pd Supported on La(Sr)-Mn-O Perovskite by Microwave Irradiation Method and its Catalytic Performances for the Methane Combustion. *Sci. Rep.* 6, 19511. doi:10.1038/srep19511

Wang, X., Huang, K., Qian, J., Cong, Y., Ge, C., and Feng, S. (2017). Enhanced CO Catalytic Oxidation by Sr Reconstruction on the Surface of La X Sr 1− X CoO 3−δ. *Sci. Bull.* 62, 658–664. doi:10.1016/j.scib.2017.03.017

Wu, H., Lei, X., Zhang, J., Yu, J., and Zhang, S. (2014). Lattice Thermal Expansion of the Solid Solutions (La1−xSmx)2Ce2O7. *Mater. Res. Bull.* 57, 320–324. doi:10.1016/j.materresbull.2014.06.016

Xia, W., Leng, K., Tang, Q., Yang, L., Xie, Y., Wu, Z., et al. (2021). Structural Characterization, Magnetic and Optical Properties of Perovskite (La1−xLnx) 0.67Ca0.33MnO3 (Ln = Nd and Sm; X = 0.0-0.5) Nanoparticles Synthesized via the Sol-Gel Process. *J. Alloys Compd.* 867, 158808. doi:10.1016/j.jallcom.2021.158808

Yanchevskii, O. Z., V'yunov, O. I., Belous, A. G., and Tovstolytkin, A. I. (2006). Crystallographic, Electrical, and Magnetic Properties of the System La0.7Sr0.3Mn1−xFexO3. *Low. Temp. Phys.* 32, 134–138. doi:10.1063/1.2171513

Yao, H. B., Li, Y., and Wee, A. T. S. (2000). An XPS Investigation of the Oxidation/corrosion of Melt-Spun Mg. *Appl. Surf. Sci.* 158, 112–119. doi:10.1016/s0169-4332(99)00593-0

Zhang, Y. B., Li, S., Sun., C. Q., and Gao, W. (2003). Possible Origin of Magnetic Transition Ordering in La2/3A1/3MnO3 Oxides (2003), 54–59.

Zhang, B., Chang, A., Zhao, Q., Ye, H., and Wu, Y. (2014). Synthesis and Thermoelectric Properties of Yb-Doped Ca0.9−x Yb X La0.1MnO3 Ceramics. *J. Elec Materi* 43, 4048–4055. doi:10.1007/s11664-014-3326-8

Conflict of Interest: The authors declare that the research was conducted in the absence of any commercial or financial relationships that could be construed as a potential conflict of interest.